

Single-hole spectral functions in 1D quantum magnets with different ground states

Sibin Yang, Gabe Schumm, Bowen Zhao, and Anders W. Sandvik*

Department of Physics, Boston University, 590 Commonwealth Avenue, Boston, Massachusetts 02215, USA

(Dated: December 25, 2025)

Thanks to improved methods for numerical analytic continuation with constraints, spectral functions with sharp features (peaks and edges) can now be extracted from imaginary-time correlation functions computed by quantum Monte Carlo (QMC) simulations. Here we test these new approaches on various one-dimensional $S = 1/2$ spin systems with a single ejected fermion, i.e., extracting the single-hole momentum (k) and energy (ω) dependent spectral function $A(k, \omega)$. We compute the distance (r) and imaginary time (τ) dependent Green's function $G(r, \tau)$ via Angelucci's canonical transformation [Phys. Rev. B **51**, 11580 (1995)] of the fermionic Hamiltonian, implementing it for stochastic series expansion QMC simulations. Our calculations of $A(k, \omega)$ focus on the different characteristics of systems with spin-charge separation and those in which a spin polaron forms instead due to effectively attractive interactions between the spin and the charge. Spin-charge separation is well established in the conventional t - J chain, which we confirm here as a demonstration of the method. Turning on a multi-spin interaction Q that eventually drives the system into a spontaneously dimerized (valence-bond solid, VBS) state, we can observe the features of spin-charge separation until the VBS transition takes place. While generally good agreement is found with the conventional analytical spin-charge separation ansatz, we point out the formation of a gap between two holon bands that in the ansatz are degenerate (crossing each other versus the momentum) at $k = 0$ and $k = \pi$. Inside the VBS phase, effectively attractive interactions may lead to the binding of the spinon and holon, of which we find evidence at large Q/J . In the statically dimerized t - J chain (i.e., with alternating strengths of the model parameters), we find equally spaced spin polaron bands corresponding to increasingly large bound states with two internal spin polaron modes—even and odd with respect to parton permutation. Our results overall demonstrate the power of modern analytic continuation tools in combination with large-scale quantum Monte Carlo simulations.

I. INTRODUCTION

The single-hole spectral function is central to understanding the nature of low-energy excitations in strongly correlated electron systems [1–16]. A prominent example of exotic excitations (beyond those of Fermi liquid theory) arises in some one-dimensional (1D) antiferromagnets, where the single-hole dynamics reveal fractionalized excitations—spinons (carrying spin $S = 1/2$) and holons (carrying charge $C = 1$)—that give rise to a continuum in the corresponding spectral function accessible in angle-resolved photoemission spectroscopy (ARPES). This spin-charge separation contrasts with the spinon-holon bound state, often called the spin polaron, which is a quasiparticle carrying both the spin and the charge compensating for the ejected electron. Spin-charge separation has been the subject of extensive theoretical investigation [17–20], with substantial confirmation by numerical model studies [21–25] and experimental observations in quasi-1D materials [26–32]. In addition to their intrinsic importance in quantum many-body physics, the work on spin-charge separation 1D systems is also strongly motivated by possible analogies in two-dimensional (2D) quantum magnets and their potential roles in high- T_c superconductivity [4, 5, 33–36].

While the density-matrix renormalization group (DMRG) method [15, 21, 22, 24, 37–45] now can provide rather accurate results for various spectral functions

of 1D systems (and some 2D systems as well [44, 45]), quantum Monte Carlo (QMC) simulations still have certain advantages, e.g., no increase in computational effort with periodic boundary conditions (momentum conservation) and, typically, reliable convergence to the ground state (with decreasing temperature) without potential trapping in metastable states. The challenge in dynamics studies with QMC is that a real-frequency spectral function $S(k, \omega)$ of an operator O has to be constructed by numerical analytic continuation of the corresponding correlation function $G(\tau) = \langle O(\tau)O(0) \rangle$ in imaginary (Euclidean) time τ . This inverse problem is “ill-posed” [46], with the frequency resolution limited by the statistical errors of the QMC data and, therefore, the outcome not being unique but to some extent depending on the method employed. With the recent development of stochastic analytic continuation (SAC) [47, 48] with physics-motivated constraints [49–54], it has become possible to resolve the sharp spectral features expected at zero temperature, edges in particular. The frequency resolution can then exceed that of DMRG calculations, where restrictions on time evolution [55] cause uncertainties in frequency space, similar to approaches working directly in frequency space [56]. Open boundaries also limit the momentum resolution.

Constrained SAC has so far been employed mainly to study the dynamic spin structure factor of various spin models [49–53]. The approach was recently also applied to the single-particle spectral function of the 2D half-filled Hubbard model, revealing novel features in the density of states [54]. This progress motivates us to revisit

* sandvik@buphy.bu.edu

also the single-hole dynamics of spin systems. The hole dynamics is then governed by the standard electron hopping terms, e.g., in the t - J model with Hamiltonian

$$H_{tJ} = -t \sum_{\langle ij \rangle, \sigma} \left(c_{i\sigma}^\dagger c_{j\sigma} + c_{j\sigma}^\dagger c_{i\sigma} \right) - J \sum_{\langle ij \rangle} P_{ij}, \quad (1)$$

where $c_{i,\sigma}^\dagger$ ($c_{i,\sigma}$) denotes the fermion creation (annihilation) operator with spin $\sigma = \uparrow, \downarrow$ on site i (implicitly acting within the restricted Hilbert space without double occupancy) and P_{ij} is the singlet projector on two sites defined as

$$P_{ij} = \frac{1}{4} n_i n_j - \mathbf{S}_i \cdot \mathbf{S}_j. \quad (2)$$

The sums in Eq. (1) typically run over nearest neighbors $\langle ij \rangle$, which will be the case considered here as well.

We consider several 1D systems, leaving the 2D case to separate publications [57, 58]. In addition to the conventional t - J chain, we also consider its extension to a dimerized chain (with alternating strong and weak couplings t_i, J_i). Moreover, we also investigate the uniform t - J - Q chain, with the Q term defined as a product of three neighboring singlet projectors;

$$H_{tJQ} = H_{tJ} - Q \sum_{\langle ijklmn \rangle} P_{ij} P_{kl} P_{mn}, \quad (3)$$

where $\langle ijklmn \rangle$ indicates six consecutive sites and the sum is over all such translated segments of sites, again with periodic boundary conditions. Beyond a critical Q/J ratio, the correlated singlet projection stabilizes a spontaneously dimerized doubly-degenerate ground state (a valence-bond solid, VBS). A VBS phase also exists with only two projectors $P_{ij} P_{kl}$ [59, 60] in the Q terms, but here we use three of them in order to achieve a more robust dimerization (maximized when $J = 0$). The dimerization transition of the host spin chain is in the same universality class as the conventional frustrated J_1 - J_2 Heisenberg chain [61–64], driven by a marginal operator as described by the level $k = 1$ Wess-Zumino-Witten field theory [65–67].

Carrying out QMC calculations of the imaginary-time correlators

$$G_{ij}(\tau) = \langle c_{j\sigma}^\dagger(\tau) c_{i\sigma}(0) \rangle, \quad (4)$$

the spectral function $A(q, \omega)$ is subsequently obtained by Fourier transformation and analytic continuation. We use the Stochastic Series Expansion (SSE) QMC method [68, 69] supplemented by a trick previously developed and used with other QMC methods [70–72]; a short overview and adaptation to SSE will be provided below. While SSE and other QMC calculations are inhibited by the sign problem [73] for systems with finite hole density and hopping beyond nearest neighbors even in 1D systems, here the sampling is performed for the sign-free host system without dopants and the injected hole exists only in a separate Hilbert space accessed for the “measurements” of the correlations.

One of the main purposes of the present work is to test the ability of constrained SAC to reproduce known or expected behaviors in systems with spin-charge separation and spin polaron formation. Beyond testing, the higher frequency resolution and the ability to resolve sharp edges and narrow quasi-particle peaks also allow us to go beyond previous studies in characterizing the excitations and their spectral signatures.

The remainder of this paper is organized as follows: In Sec. II, we briefly outline the main steps for evaluating the single-hole imaginary-time correlation function using SSE QMC simulations and introduce the basic principles of unconstrained SAC. The single-hole spectral function $A(k, \omega)$ of the uniform t - J and t - J - Q chains is presented in Sec. III, where constrained sampling in SAC is also introduced and results obtained with different constraints are compared and discussed. In Sec. IV, we analyze multi-band spin-polaron features observed in the dimerized chain. Sec. V provides a summary of our findings and the advantages of constrained SAC.

II. METHODS

In Sec. II A, we explain the procedure for calculating the single-hole imaginary-time Green’s function $G(i, j, \tau)$, adapting the procedures of Refs. [70–72] to the SSE representation of the imaginary-time continuum (instead of the time-discretized world-line formalism used previously). We then perform a Fourier transform to obtain $G(k, \tau)$, which serves as the input for SAC after an additional processing step involving constructing and diagonalizing the covariance matrix. In Sec. II B, we summarize the basic aspects of the SAC method without sampling constraints. The constrained versions of SAC will be discussed in their respective contexts of different excitations with sharp features in the frequency dependence.

A. Single-hole Green’s function

For clarity, we here focus on the t - J model, Eq. (1), and the almost trivial extension to the t - J - Q model will be explained later. The spin operators now have to be defined explicitly in terms of the fermionic operators:

$$\begin{aligned} \mathbf{S}_i &= (S_i^x, S_i^y, S_i^z) \\ &= \frac{1}{2} (c_{i\uparrow}^\dagger c_{i\downarrow} + c_{i\downarrow}^\dagger c_{i\uparrow}, i(c_{i\downarrow}^\dagger c_{i\uparrow} - c_{i\uparrow}^\dagger c_{i\downarrow}), n_{i\uparrow} - n_{i\downarrow}). \end{aligned} \quad (5)$$

In order to simplify the Hamiltonian, we next perform Angelucci’s canonical transformation [70]:

$$c_{i\uparrow}^\dagger = \gamma_{i,+} f_i - \gamma_{i,-} f_i^\dagger, \quad c_{i\downarrow}^\dagger = \sigma_{i,-} (f_i + f_i^\dagger), \quad (6)$$

where f_i are standard anti-commuting spinless fermions, $\{f_i^\dagger, f_j\} = \delta_{ij}$, and

$$\gamma_i^\pm = (1 \pm \sigma_i^z)/2, \quad (7a)$$

$$\sigma_i^\pm = (\sigma_i^x \pm i\sigma_i^y)/2, \quad (7b)$$

where $\vec{\sigma}$ are the Pauli matrices, with σ_i^\pm the corresponding spin raising and lowering operators. Then, the Hamiltonian becomes:

$$H = t \sum_{\langle ij \rangle} \Lambda_{ij} (f_i^\dagger f_j + f_j^\dagger f_i) + \frac{J}{2} \sum_{\langle ij \rangle} \Delta_{ij} (\Lambda_{ij} - 1), \quad (8)$$

where

$$\Lambda_{ij} = (1 + \vec{\sigma}_i \cdot \vec{\sigma}_j)/2 \quad (9a)$$

$$\Delta_{ij} = (1 - n_i - n_j). \quad (9b)$$

Note that the J term is now expressed solely with the spin operators and the diagonal fermion number operators, $n_i \in \{0, 1\}$, while the kinetic t term mixes spin interactions and fermion hopping. In the absence of holes, the Hamiltonian is still identical to that of the $S = 1/2$ antiferromagnetic Heisenberg model.

The fermion operators can be taken to represent degrees of freedom different from the spins but with an explicit constraint that is conveniently taken into account by defining the single-site Hilbert space with its three states as

$$|\eta_i\rangle = |n_i, z_i\rangle \in \{|0, \uparrow\rangle_i, |0, \downarrow\rangle_i, |1, \uparrow\rangle_i\}, \quad (10)$$

i.e., the hole can be regarded as replacing an \uparrow spin. The ‘‘missing state’’ $|1, \downarrow\rangle_i$ represents a doubly occupied site in the more general treatment of the Hubbard model [70]. It will also be useful to introduce a notation for the further restricted Hilbert space without a hole

$$|\alpha_i\rangle = |0, z_i\rangle \in \{|0, \uparrow\rangle_i, |0, \downarrow\rangle_i\}, \quad (11)$$

which is just the standard $S = 1/2$ spin space that will be used in the SSE sampling of the spin part of the Hamiltonian in the absence of holes. The Hilbert space including a single hole in Eq. (10) will here be accessed only when measuring the Green’s function.

Three types of operators in the Hamiltonian can be identified that will be sampled in the SSE scheme:

$$-H_{1,ij} = J\Delta_{ij}(1 - \sigma_i^z \sigma_j^z)/4, \quad (12a)$$

$$-H_{2,ij} = -(\sigma_j^+ \sigma_i^- + \sigma_j^- \sigma_i^+) \times [J\Delta_{ij}/2 + t(f_i^\dagger f_j + f_j^\dagger f_i)], \quad (12b)$$

$$-H_{3,ij} = -(t/2)(1 + \sigma_i^z \sigma_j^z)(f_i^\dagger f_j + f_j^\dagger f_i) + tI_{ij}, \quad (12c)$$

and the t - J Hamiltonian is then

$$H = - \sum_{a=1}^3 \sum_{\langle i,j \rangle} (-H_{a,ij}), \quad (13)$$

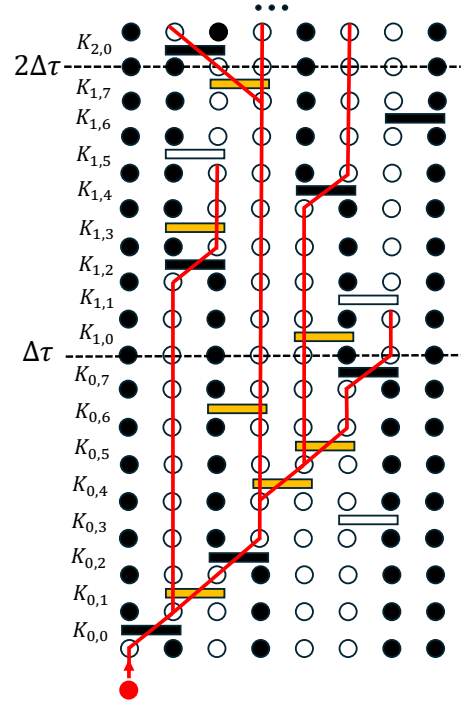


FIG. 1. Illustration of an SSE configuration of a system with eight spins and time slices including $M = 8$ operators in Eq. (16). Spins \uparrow and \downarrow are represented by open and solid circles, respectively, and the operators $K_{l,s}$ shown as bars from the sets defined in Eqs. (12), with the operator types corresponding to colors as follows: white for $a = 1$, black for $a = 2$, and yellow for $a = 3$. No fill-in unit operators are included here but will appear in actual SSE configurations. The red dot represents an injected hole replacing the \uparrow spin at site 1, and the red line illustrates the different paths this hole can take upon evolution in imaginary time. Note that the hole in this representation can propagate only on sites with \uparrow spins, reflecting the definition of the three-state basis, Eq. (10).

where the first negative sign will be canceled by the minus sign appearing in the density operator $e^{-\beta H}$. In Eq. (12c), I_{ij} is simply a unit operator associated with the sites i, j whose role will become clear below.

To measure the Green’s function at L predefined time slices, which we here take equally spaced at separation $\Delta\tau = \beta/L$, it is convenient to expand the individual slice operators $e^{-\Delta\tau H}$ instead of the single expansion of the full density operator;

$$e^{-\beta H} = (e^{-\Delta\tau H})^L = \sum_K \left[\prod_{l=1}^L \frac{\Delta\tau^{n_l}}{n_l!} \right] \prod_{l=1}^L \prod_{s=1}^{n_l} K_{l,s}, \quad (14)$$

where the operators $K_{l,i}$ are drawn from the set of operators defined in Eqs. (12), i.e., $K_{l,s} \in \{-H_{a,ij}\}$. As usual [69], the expansions are cut at some order $n_l = M$ beyond which the series is in practice completely converged. Unit operators $K_{l,s} \equiv I$ separate from the Hamiltonian operators are used to randomly augment the terms with $n_l < M$ to length M , with n_l still counting the number

of Hamiltonian operators in the expansion at slice l . The combinatorial factor is then modified to

$$C(\{n_l\}) = \prod_{l=0}^{L-1} \Delta_\tau^{n_l} \frac{(M - n_l)!}{M!}, \quad (15)$$

and the partition function $Z = \text{Tr}\{e^{-\beta H}\}$ is further sampled in a chosen basis, here the spin states $|\alpha\rangle = \prod |\alpha_i\rangle$:

$$Z = \sum_{\alpha, K} C(\{n_l\}) \left\langle \alpha \left| \prod_{l=0}^{L-1} \prod_{s=1}^M K_{l,s} \right| \alpha \right\rangle, \quad (16)$$

where now $K_{l,s} \in \{-H_{a,ij}, I\}$. In practice $n_l < M$ is required to hold for all terms generated by choosing M sufficiently large during the equilibration of the simulation, so that the truncation does not introduce any error.

The expansion in Eq. (16) is positive definite for any antiferromagnetic spin model on a bipartite graph, on account of the trace in this case requiring an even number of the operators $H_{2,ij}$ to be present in Eq. (12b). Apart from the unit operators $H_{3,ij}$ in Eq. (12c), which are present even in the absence of holes, this is just the standard SSE formulation of the problem, and inclusion of the $H_{3,ij}$ operators in the sampling is trivial. Fig. 1 shows an illustration of an SSE configuration, also including an injected hole that we consider next. In this illustration we have not indicated any fill-in unit operators in the truncated expansion, since they do not affect the hole motion. Actual SSE configurations with the cut-off M properly adjusted would have a significant fraction of unit operators (typically about 20-30% [69]) in all the time slices.

Since no double-occupancy is allowed in the host spin model, the one-hole Green's function defined in Eq. (4) is expressed only with particle destruction at a site i at some time τ_0 , here taken as $\tau_0 = 0$ (later averaging over several slices for the injection), and creation at a site j at a later time $\tau_0 + \tau$. Let us examine the action of the fermion destruction (hole creation) operators, the conjugates of Eq. (6), on the single-site basis states in the

notation of Eq. (10);

$$c_{i\uparrow}|0, \uparrow\rangle = f_i^\dagger|0, \uparrow\rangle = |1, \uparrow\rangle, \quad (17a)$$

$$c_{i\downarrow}|0, \downarrow\rangle = \sigma_i^+ f_i^\dagger|0, \downarrow\rangle = |1, \uparrow\rangle, \quad (17b)$$

$$c_{i\uparrow}|0, \downarrow\rangle = 0, \quad (17c)$$

$$c_{i\downarrow}|0, \uparrow\rangle = 0. \quad (17d)$$

Thus, the hole creation on an \uparrow site is slightly simpler and we will consider only that case, knowing that destruction of a \downarrow will lead to the same result by symmetry. Given the spin inversion symmetry of the models studied here, for the purpose of improved sampling statistics, hole creation on also \downarrow sites can be considered by applying $c_{i\uparrow}$ to the inverted spin configuration in case of a \downarrow , spin on i . With an \uparrow spin at i we have

$$\begin{aligned} G(i, j, \tau) &= \langle c_{i\uparrow}^\dagger(\tau) c_{j\uparrow}(0) \rangle = \langle f_i(\tau) f_j^\dagger(0) \rangle \\ &= \frac{1}{Z} \text{Tr} \left[e^{-(\beta-\tau)\mathcal{H}} f_i e^{-\tau\mathcal{H}} f_j^\dagger \right], \end{aligned} \quad (18)$$

where the trace is over all states not containing a hole, i.e., the α basis defined in Eq. (11). Between the creation and destruction operators, the evolved states contain a single hole and the basis states for a system of N sites is a product of a single-hole state $\eta_i = |1, \uparrow\rangle_i$ and $N - 1$ spin states, $\prod |\alpha_j\rangle, j \neq i$. We refer to generically to these states as $|\eta\rangle$.

Restricting the time τ to an integer L_τ of time slices, we proceed in analogy with the partition function in Eq. (14), writing

$$G(i, j, \tau) = \frac{1}{Z} \text{Tr} \left[\prod_{l=L_\tau+1}^L e^{-\Delta\tau\mathcal{H}} f_i \prod_{l=1}^{L_\tau} e^{-\Delta\tau\mathcal{H}} f_j^\dagger \right]. \quad (19)$$

and then inserting complete sets of states between all the exponential operators. Taking the trace and Taylor expanding all exponentials we have

$$\begin{aligned} G(i, j, \tau) &= \frac{1}{Z} \sum_{\alpha\eta} \langle \alpha_0 | e^{-\Delta\tau H} | \alpha_{L-1} \rangle \dots \langle \alpha_{L_\tau+1} | e^{-\Delta\tau H} | \alpha_{L_\tau} \rangle \langle \alpha_{L_\tau} | f_i e^{-\Delta\tau H} | \eta_{L_\tau-1} \rangle \dots \langle \eta_1 | e^{-\Delta\tau H} f_j^\dagger | \alpha_0 \rangle \\ &= \frac{1}{Z} \sum_{\alpha, K} C(\{n_l\}) \langle \alpha_{0,0} | K_{L,M} | \alpha_{L-1,M} \rangle \dots \langle \alpha_{0,2} | K_{1,2} | \alpha_{0,1} \rangle \langle \alpha_{0,1} | K_{1,1} | \alpha_{0,0} \rangle \times \\ &\quad \sum_{\eta'} \frac{\langle \alpha_{L_\tau,0} | f_i K_{L_\tau,M} | \eta_{L_\tau-1,M-1} \rangle \dots \langle \eta_{0,2} | K_{1,2} | \eta_{0,1} \rangle \langle \eta_{0,1} | K_{1,1} f_j^\dagger | \alpha_{0,0} \rangle}{\langle \alpha_{L_\tau,0} | K_{L_\tau,M} | \alpha_{L_\tau-1,M-1} \rangle \dots \langle \alpha_{0,2} | K_{1,2} | \alpha_{0,1} \rangle \langle \alpha_{0,1} | K_{1,1} | \alpha_{0,0} \rangle} \\ &= \sum_{\alpha, K} W(\alpha, K) G_{ij\tau}(\alpha, K). \end{aligned} \quad (20)$$

Here $W(\alpha, K)$ is defined by the expression inside the

summation on second line and is identical to the sampling

weight of the partition function Eq. (16). The estimator $G_{ij\tau}(\alpha, K)$ for the Green's function is the entire sum over states $|\eta'\rangle$ that represent the single-hole basis states inserted between the time slices where a hole is present. The reason that this expression works is that the operator strings that contribute to the partition function of the spin system are exactly the same ones that contribute when a single hole is present. The matrix elements are different however, as different parts of the Hamiltonian operators in Eq. (12) are active in propagating a basis state to another basis state (with other parts destroying the state).

With the two-body operators of the t - J model, the bra and ket states appearing in non vanishing matrix elements $\langle\alpha'|H_{a,ij}|\alpha\rangle$ and $\langle\eta'|H_{a,ij}|\eta\rangle$ differ at most at two sites i, j . Thus, the non-trivial elements can be expressed as 2×2 matrices in the relevant subspaces and can easily be read from Eq. (12). For clarity, we here write these matrices together with the subspace states in question, indicated on the right side of the respective matrices. Those in the sector with no holes are

$$-H_{1,ij} = \frac{J}{2} \begin{bmatrix} 1 & 0 \\ 0 & 1 \end{bmatrix} \begin{array}{l} |0 \uparrow, 0 \downarrow\rangle \\ |0 \downarrow, 0 \uparrow\rangle \end{array} \quad (21a)$$

$$-H_{2,ij} = -\frac{J}{2} \begin{bmatrix} 0 & 1 \\ 1 & 0 \end{bmatrix} \begin{array}{l} |0 \uparrow, 0 \downarrow\rangle \\ |0 \downarrow, 0 \uparrow\rangle \end{array} \quad (21b)$$

$$-H_{3,ij} = tI, \quad (21c)$$

where the identity operator on the last line is defined in the full 2-spin space $|\sigma_i^z, \sigma_j^z\rangle$. In the one-hole sector

$$-H_{1,ij} = 0 \quad (22a)$$

$$-H_{2,ij} = -t \begin{bmatrix} 0 & 1 \\ 1 & 0 \end{bmatrix} \begin{array}{l} |1 \uparrow, 0 \downarrow\rangle \\ |0 \downarrow, 1 \uparrow\rangle \end{array} \quad (22b)$$

$$-H_{3,ij} = t \begin{bmatrix} +1 & -1 \\ -1 & +1 \end{bmatrix} \begin{array}{l} |0 \uparrow, 1 \uparrow\rangle \\ |1 \uparrow, 0 \uparrow\rangle \end{array} \quad \text{or} \quad (22c)$$

$$-H_{3,ij} = t \begin{bmatrix} 1 & 0 \\ 0 & 1 \end{bmatrix} \begin{array}{l} |1 \uparrow, 0 \downarrow\rangle \\ |0 \downarrow, 1 \uparrow\rangle \end{array}. \quad (22d)$$

Here 0 in Eq. (22a) implies that this operator will destroy any state with a hole; thus, a hole propagation path will terminate when an $H_{1,ij}$ operator (corresponding to a diagonal spin interaction) is encountered. Another key aspect of the hole propagation is that $H_{3,ij}$ when both spins are \uparrow in Eq. (22c) leads to branching, with a path splitting into one branch continuing to evolve on the same site while in the other branch the hole jumps to the second site of the operator. This operator can also appear between two anti-parallel spins, in which case the hole can only continue to propagate on the \uparrow site, as indicated by the second matrix for this case in Eq. (22d). The case of the hole entering this operator at the \downarrow spin is excluded from the outset (and would lead to zero). The initial part of a branching hole path is shown in Fig. 1.

The contributions to the Green's function in Eq. (20) are products of matrix element ratios $R_{a,ij}$, $a = 1, 2, 3$,

which from Eq. (21) and Eq. (22) are,

$$R_{1,ij} = 0 \quad (23a)$$

$$R_{2,ij} = \frac{2t}{J} \begin{bmatrix} 0 & 1 \\ 1 & 0 \end{bmatrix} \begin{array}{l} |1 \uparrow, 0 \downarrow\rangle \\ |0 \downarrow, 1 \uparrow\rangle \end{array} \quad (23b)$$

$$R_{3,ij} = \begin{bmatrix} +1 & -1 \\ -1 & +1 \end{bmatrix} \begin{array}{l} |0 \uparrow, 1 \uparrow\rangle \\ |1 \uparrow, 0 \uparrow\rangle \end{array} \quad \text{or} \quad (23c)$$

$$R_{3,ij} = \begin{bmatrix} 1 & 0 \\ 0 & 1 \end{bmatrix} \begin{array}{l} |1 \uparrow, 0 \downarrow\rangle \\ |0 \downarrow, 1 \uparrow\rangle \end{array}. \quad (23d)$$

With a hole injected in an SSE configuration at a specific site i at an allowed τ point (at which the spin is in the \uparrow state), the contributions from all possible paths can be summed up in the following way: A vector v with N elements (the number of spins), is initialized with all zeros, except for 1 at the position i corresponding to the \uparrow site into which the hole is injected in the state $|\alpha_{0,0}\rangle$ that is stored. The SSE operator string is then traversed, updating the stored spin state according to the operators encountered sequentially according to in Eq. (20). For each Hamiltonian operator (disregarding the trivial unit operators used to augment the operator sequence), the vector v is multiplied by the corresponding matrix $R_{a,ij} \otimes I_{ij}$, where I_{ij} formally indicates the part of the $N \times N$ matrix comprising only of $N-2$ diagonal unit elements. For each entire time slice traversed, the vector elements $v(j)$ represent the estimators of $G(i, j, \tau)$ for all j when the starting position is i . Arranging the vectors for all allowable injection sites as the columns of an $N/2 \times N$ matrix, with the i th column initialized with 1 in the element corresponding to the location of the i th \uparrow spin as above (and note that the number of \uparrow sites is always $N/2$ when the temperature is low enough for only the singlet ground state of the spin system to be sampled), the estimators for all $G(i, j, \tau)$ are generated from a single scan of the SSE operators. The computational effort then scales as $N^2\tau$, with $N\tau$ coming from the scaling $N\beta$ of the total number of operators in the SSE expansion. The scaling is the same as in the previous implementations within the discrete (Trotter approximated) world-line method [71, 72] but in the SSE approach there are no discretization errors. The results can also be averaged over injections at different time slices, which leads to another factor β in the formal scaling but also provides additional statistics if the injection slices are sufficiently far apart.

Moving on to the t - J - Q model, SSE simulations of various J - Q model require only minor modifications of the Heisenberg (J model) algorithm and have been described in detail in previous works [69]. With Q terms defined as products of the singlet projectors in Eq. (3), they can be treated the same way as the J -operators. The hopping terms need still be combined only with the J -operators as in Eqs. (12), and then no holes are allowed on the additional operators corresponding to the Q terms. The modification of the estimator for the Green's function is then trivial—any hole branch entering a Q operator is terminated, with a corresponding 0 in the matrix element ratio as in Eq. (23a). Another option is to divide

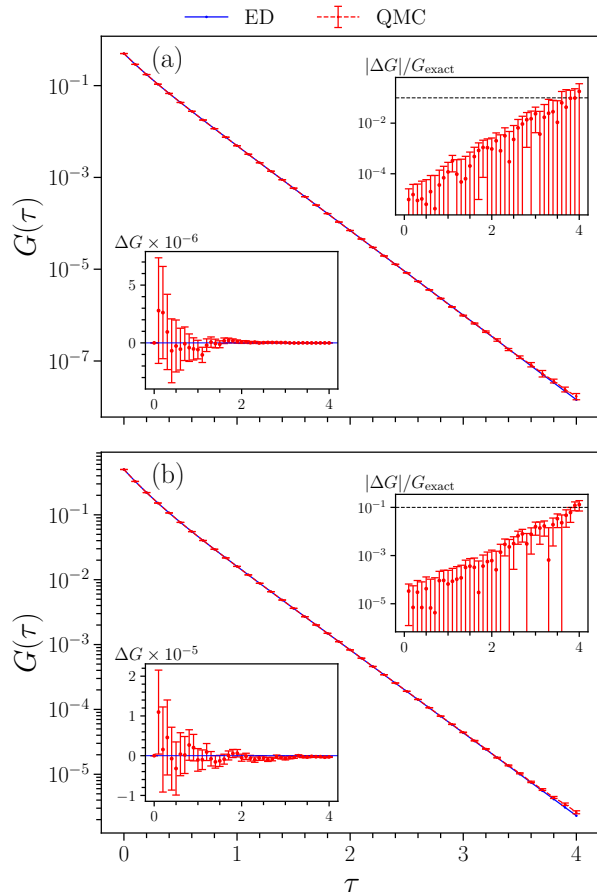


FIG. 2. Comparisons of the exact $k = \pi/2$ Green's function (blue curve, from full diagonalization of H) of $N = 8$ chains and corresponding SSE results (red points with error bars) for (a) the standard t - J chain at $t = 1$, $J = 4$ and (b) The t - J - Q chain with $t = 1$, $J = 2$, and $Q = 0.5$. The left and right insets show, respectively, the absolute and relative difference between the SSE data and the exact results. In the analytic continuation we use only data points for which the statistical error (one standard deviation of the mean) is less than 0.1, which corresponds to a similar relative error with respect to the exact value, indicated here with dashed lines. Note that the log scale in the insets showing $|\Delta G|/G_{\text{exact}}$ does not visually reflect the size of the lower part of the error bar (one standard deviation of the mean). In (a) the deviation from the exact value at $\tau = 4$ is 1.0 standard deviation, while in (b) it is 2.1 standard deviations. The deviations overall are statistically likely.

the t terms also over the Q interactions. While we have not made extensive comparisons, limited tests indicate that it is somewhat more efficient to combine the t -terms only with the J -interactions, unless J/Q is very small.

In practice, the relative statistical errors of $G(k, \tau)$ (with k denoting the dimensionless momentum after Fourier transforming SSE results for all site pairs i, j) grow with increasing τ and the calculation is therefore restricted to a number of τ values below a cut-off τ_{max} . In the work presented here, we typically take $t = 1$ as the

energy scale, set the time slice to $\Delta\tau = 0.1$ and generate data up to $\tau = 4$ or $\tau = 8$. We also average over imaginary time, stepping over a number of time slices corresponding to the maximum τ value used. Aiming for the ground state, we set the inverse temperature to a multiple of the system size N (typically $\beta = 2N$), sufficiently large for no statistically significant finite-temperature effects to remain up to τ_{max} . To test the code, we have compared with exact diagonalization of small systems; two illustrative examples of Green's function $G(k, \tau)$ in momentum space are shown in Fig. 2. Here it is interesting to note that the magnitude of the statistical errors actually decreases with increasing τ , reflecting the improved statistics as the hole path branches out and eventually terminates—the averages at large τ are then over small values in many elements in the vector v representing the propagated hole amplitudes, instead of a small number of larger values at small τ . The relative statistical errors still increase with τ .

B. Spectral function

Here we consider the $T = 0$ spectral function of the single-hole operator $O = c_{k,\uparrow}$, which in the Lehman representation is given by

$$A(k, \omega) = \pi \sum_m |\langle m, N-1 | c_{k,\uparrow} | 0, N \rangle|^2 \delta(\omega - \epsilon_m). \quad (24)$$

Here, $|0, N\rangle$ denotes the ground state of the spin model (corresponding to a half-filled Hubbard model with large repulsion U) with N spins and ground state energy E_0 (and the momentum of this state is $k = 0$ for a chain of length $L = 4n$ for integer n), while $|m, N-1\rangle$ are the states with a hole and energy E_m (all of which have momentum $-k$), and $\epsilon_m = E_m - E_0$ is the excitation energy. The corresponding correlation function at momentum k and imaginary time τ

$$G(k, \tau) = \langle c_{k,\uparrow}^\dagger(\tau) c_{k,\uparrow}(0) \rangle, \quad (25)$$

is obtained by Fourier transforming the real-space correlators discussed above in Sec. II A. The relation between $G(k, \tau)$ and the real-frequency spectral function $A(k, \omega)$ at $T = 0$ is

$$G(k, \tau) = \frac{1}{\pi} \int_{-\infty}^{+\infty} d\omega A(k, \omega) e^{-\tau\omega}, \quad (26)$$

which we invert using the SAC method.

We here discuss SAC in its most generic (unconstrained) form, where a set of a large number N_ω of δ -functions is sampled and (suppressing the k label here)

$$A(\omega) = \sum_{i=1}^{N_\omega} a_i \delta(\omega - \omega_i), \quad (27)$$

typically with N_ω of order 10^3 or larger. The frequencies ω_i live effectively in the continuum, in practice on

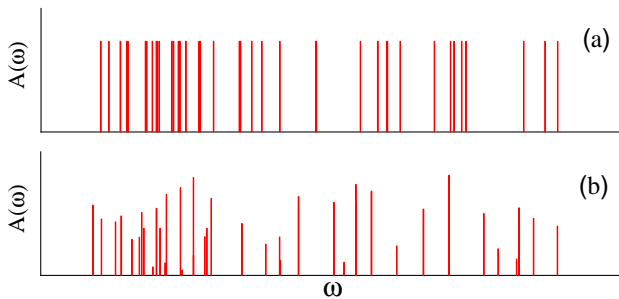


FIG. 3. Two parameterizations of the spectral function $A(\omega)$ used in unconstrained SAC with a large number N_ω (typically thousands) of δ -functions in the frequency continuum (in practice on a grid with very small spacing; $\Delta_\omega = 10^{-5}$ or smaller). In (a), each δ -function carries the same fixed weight N_ω^{-1} of the normalized spectrum and only the locations ω_i are sampled, while in (b) also the amplitudes are sampled, with the total spectral weight conserved.

a very fine grid between bounds ω_{\min} and ω_{\max} beyond which the spectral weight is negligible. The kernel $e^{-\tau\omega_i}$ in Eq. (26) can then be precomputed for all ω_i and τ points used (typically with tens of points τ_i). Two commonly used versions of unconstrained SAC parametrizations of the spectral function are illustrated in Fig. 3; one where the amplitudes are fixed uniformly at $a_i = 1/N_\omega$ [74] and the other where the amplitudes are also sampled along with the frequencies ω_i [48]. The configurational entropies of these parametrizations are different [51, 75], leading to slightly different outcomes for the mean spectral density accumulated in a histogram. It is also possible to define the frequencies ω_i on a fixed grid and only sample the amplitudes [47], but the entropic pressures of this parametrization are more prone to produce spurious features and distortions than those in Fig. 3 [51].

The spectrum is sampled with a Boltzmann-like probability distribution,

$$P(A|\bar{G}) \propto \exp\left(-\frac{\chi^2}{2\Theta}\right), \quad (28)$$

with $\chi^2/2$ playing the role of the energy of the system at a fictitious temperature Θ , the optimal value of which is determined by a simple criterion that balances both the goodness-of-fit $\langle\chi^2\rangle$ (ensuring a statistically acceptable value) and the entropy (avoiding over-fitting to the statistical noise in G) [51, 52, 74]:

$$\langle\chi^2(\Theta)\rangle = \chi_{\min}^2 + a\sqrt{2\chi_{\min}^2}. \quad (29)$$

Here a is a constant of order unity and χ^2 is the goodness of fit to the QMC data defined with the full covariance matrix C as

$$\chi^2 = \sum_i \sum_j (G_i - \bar{G}_i)[C^{-1}]_{ij}(G_j - \bar{G}_j), \quad (30)$$

where, $G_i \equiv G(\tau_i)$ are the Green's function values obtained from $A(\omega)$ using Eq. (26) for the chosen set of N_τ

time points τ_i while $\bar{G}_i \equiv \bar{G}(\tau_i)$ are the mean data from a QMC simulation. The covariance matrix with elements C_{ij} are computed from averages G_i^b for a large number of data bins $b = 1, \dots, N_B$;

$$C_{ij} = \frac{1}{N_B(N_B - 1)} \sum_{b=1}^{N_B} (G_i^b - \bar{G}_i)(G_j^b - \bar{G}_j). \quad (31)$$

Here N_B should be much larger than the number of τ points N_τ , so that the covariance matrix itself is statistically reliable [46]. The significant covariance of the data set also implies that already a rather small N_τ (e.g., of order ten or a few tens of points) effectively exhausts the limited information content in the noisy data set (even with QMC data of the best possible quality). The number of τ points computed in the QMC simulations can be larger than the finally used N_τ based on initial tests. However, computing too many times is also not desirable, given the scaling of the computational effort for each $G(\tau_i)$.

Further technical details, recent developments, and applications of SAC are discussed in Refs. [51–54]. In the following results sections, not only the unconstrained SAC but also more advanced constrained ones will be implemented to enable detection of the sharp features expected in single-hole spectral functions at $T = 0$ when the excitations are either spin-charge fractionalized or confined spin polarons.

III. UNIFORM t - J AND t - J - Q CHAINS

According to the spin-charge separation ansatz [10], excitations formed by hole injection by the operator $c_{k,\sigma}$ are fractionalized in the t - J chain, thus leading to a continuum of spinon and holon contributions to $A(k, \omega)$. The spectral bounds are expected to be manifested as edges with power-law divergences at the lowest and highest combined spinon and holon energies. Here we study the standard t - J chain as well as the t - J - Q chain, in the latter first with Q/J tuned to the dimerization transition point $(Q/J)_c$ and then inside the VBS phase for $Q/J > (Q/J)_c$. At $(Q/J)_c$, the logarithmic corrections associated with the marginally irrelevant operator in the host Heisenberg chain ($t = 0$ and no holes) vanishes, changing signs and becoming marginally relevant in the VBS phase [76, 77]. While it is not clear how the logarithmic corrections affect the single-hole spectral function, given that the spin-charge separation ansatz is only an approximation (a mean-field solution of the Hamiltonian written with “slave bosons”) [10, 71] and does not account for subtleties such as logarithmic corrections. It is nevertheless interesting to study the t - J - Q chain at the special point $(Q/J)_c$.

At the mean-field level, the spinon and the holon propagate with independent momenta q_s and q_h , respectively,

with dispersion relations

$$\epsilon_s = -J_s \cos(q_s), \quad (32a)$$

$$\epsilon_h = -t_h \cos(q_h). \quad (32b)$$

When the hole operator c_k acts on the ground state of the spin chain, a holon and an anti-spinon are created. Thus, the total momentum is $k = q_h - q_s$ and the energy is $E_k = \epsilon_h - \epsilon_s$. The parameters t_h and J_s are equal to $2t$ and J in the mean-field Hamiltonian according to Ref. [71], but instead of the bare values they can also be taken as phenomenological parameters. In the case of the t - J - Q chain, we have not derived the mean-field expressions for t_s and J_s but simply take them as fitting parameters. In all cases, we also have to add a constant to the holon dispersion, corresponding to a chemical potential, $\epsilon_h \rightarrow \epsilon_h + \mu$, where we also treat μ as a fitting parameter.

While only a single hole is injected into the host spin system and only one holon is created, the resulting fermionic anti-spinon is taken from a Fermi sea of already existing spinons. Furthermore, a so-called phase-string effect modifies the spectral weight density, leading to singularities in $A(k, \omega)$ beyond a sharp edge with divergent spectral weight density that is present already with the bare spinon and holon. Thus, the behavior is quite complex even at the mean-field level. We refer to the literature [10, 71] for details and only quote results required to motivate a modified SAC parametrization used below.

As a consequence of the restriction of the spinon to its Fermi sea, there is a special momentum k_0 , with $\cos(k_0) = J_s/t_h$, such that the lower edge of the compact support of $A(k, \omega)$ is given by a function $-F_k$ for $k < k_0$ and the upper edge is at F_k for $k_0 < k < \pi$, where

$$F_k = \sqrt{J_s^2 + t_h^2 - 2t_h J_s \cos(k)}. \quad (33)$$

Because of the phase-string effect, these edges are associated with power-law singularities. The remaining edges of the compact support outside the regions defined by k_0 above are given by $E_k = \pm t_h \sin(k)$, arising from holons with momentum $q_h = k + q_s$, $q_s = \pm\pi/2$ (i.e., $\epsilon_s = 0$), and these are also preceded by power-law divergent spectral weight. Thus, for all k , there are altogether three peaks versus ω , though close to k_0 the third peak will be very close to E_k and, therefore, very hard to separate as an individual feature in numerical studies.

A. Critical phase and dimerization point

We first consider the t - J chain with $t = 1$ and $J = 0.4$, which is one of the cases used in previous QMC calculations with analytic continuation by the maximum-entropy method by Brunner et al. [71] for chain lengths up to $L = 128$. Recently, Wrzosek et al. presented exact diagonalization (ED) results for the same model parameters and a system of size $L = 28$ [25], larger than in previous (ED) studies. All results here will be for $L = 64$, even

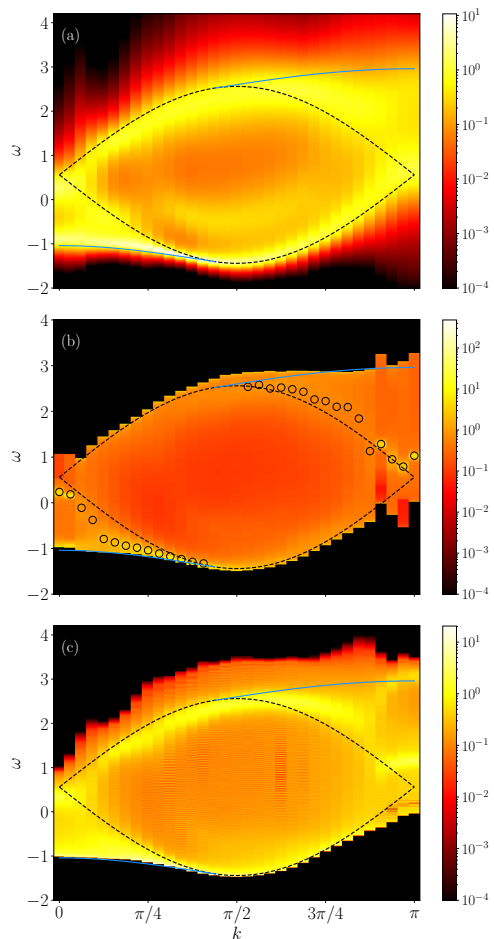


FIG. 4. Spectral function $A(k, \omega)$ of the $L = 64$ t - J chain with $t = 1$ and $J = 0.4$ obtained by SAC with one unconstrained and two constrained δ -function parametrizations. (a) with unconstrained variable amplitudes as in Fig. 3(b). (b) with a double edge representing the spectral bounds and unconstrained contributions between the edges, combining Figs. 6(a), 6(b), and 6(c). In (c), the single-edge constraint illustrated in Fig. 6(a) has been combined with unconstrained δ -functions above the edge as in Fig. 6(b). The black dashed lines show the upper and lower holon branch (on which the spinon has momentum $k = \pi/2$ and energy 0) according to the spin-charge separation ansatz. The blue solid lines show the lowest and highest energies of the combined spinon and holon excitations when not coinciding with the holon branches. These predictions are based on the dispersion relations in Eqs. (32) with $J_s = J$ and $t_h = 2t$. The circles in (b) show the locations of local maximums inside the continuum that we identify with the holon branches.

though much larger systems can be accessed with our methods. Based on tests, we do not see significant finite-size changes for $L > 64$, and since high-precision $G(k, \tau)$ results are required for reliable analytic continuation it is better to use moderate system sizes for which smaller statistical errors can be achieved at reasonable computational cost. Fig. 4 shows our analytically continued results based on three different SAC parametrizations,

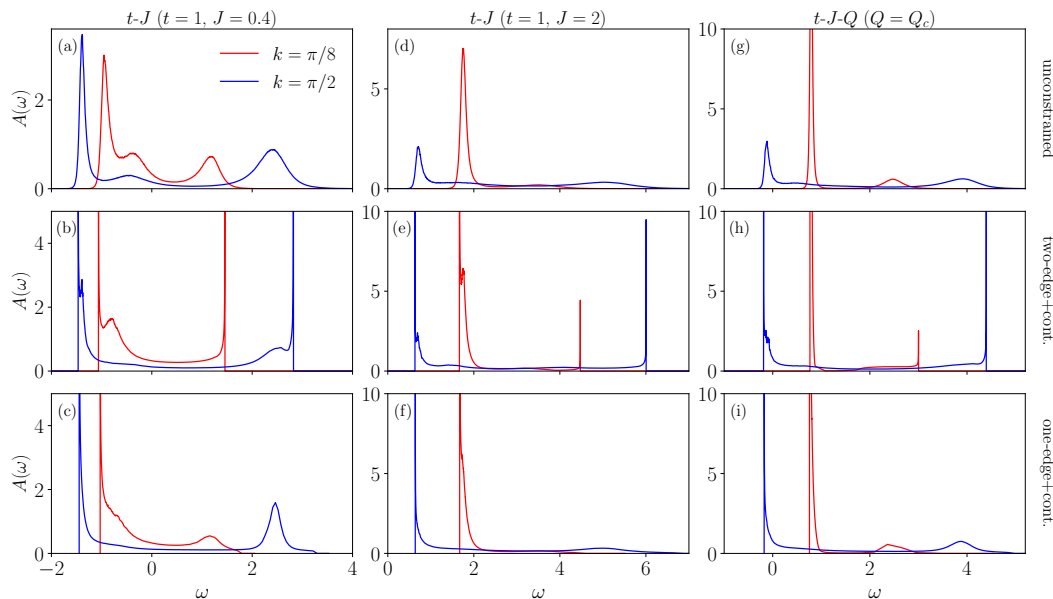


FIG. 5. Spectral profiles for fixed $k = \pi/8$ (red curves) and $\pi/2$ (blue curves) for three different parameter sets of the t - J ($Q = 0$) and t - J - Q models, as indicated on top of the respective columns. In each case, three different SAC parametrizations were used; unconstrained in (a),(d),(g), double-edge in (b),(e),(h) and lower edge only in (c),(f),(i). Parameter sets correspond to the heat-map representation of the entire spectral function in Figs. 4, 7, and 8.

graphing the complete spectral function for all $0 \leq k \leq \pi$. The logarithmic scale in the heat map spans values down to 10^{-4} , such that black regions correspond to negligible or vanishing spectral weight. To complement the heat map representation of $A(k, \omega)$, in Figs. 5(a)-(c) we show examples of spectral profiles graphed on linear scale for two values of k .

Figs. 4(a) and Fig. 5(a) show results of unconstrained sampling with both frequencies and amplitudes updated, corresponding to Fig. 3. The expected singularities discussed above are marked, here with $t_h = 2t$ and $J_s = J$, which represent very close to optimal parameters for this rather small value of J/t (where the ansatz is expected to work the best). The bright bands in the SAC spectra coincide very closely with the predicted spectral bounds, and there is relatively little spectral weight above the predicted upper bound. There is elevated spectral weight around the predicted holon singularities at $\omega_k = \pm t_h \sin(k) + \mu$ (with μ adjusted for best fit) also when these singularities are inside the continuum. Overall, the results look rather similar to the exact diagonalization results for $L = 28$ [25], where additional “mini bands” are seen inside the continuum due to the small number of δ functions making up the exact spectral function, Eq. (24), for a small system. The SAC method cannot resolve such fine structure, which is anyway expected to smoothen out to a true continuum in the thermodynamic limit. With unconstrained sampling, the expected pure holon singularity for $k < k_0$ (where the spinon momentum $k_s = \pi/2$ and, therefore, $\epsilon_s = 0$) is only marginally resolved as a broad peak, similar to previous results obtained with the maximum-entropy method [71].

In Fig. 4(a), there is also a weaker broad band close to the lower holon edge. It is known that numerical analytic continuation, with SAC or other related techniques, e.g., the maximum-entropy method [46], are prone to producing artificial peaks in spectral functions (versus ω for fixed k) with QMC imaginary-time data $G(k, \tau)$ of typical statistical quality. It has been shown that such peaks often are secondary, spurious features resulting from excessive broadening of peaks at lower energy [51]. In the present case, the exact spectrum should have a sharp lower edge but it is broadened significantly by SAC (as with any conventional analytic continuation method); in particular, spectral weight is present below the edge. The wrongly distributed weight leads to $G(k, \tau)$ decaying slower than it should for large τ , and to partially compensate (in order for the sampled spectrum to fit the data) the peak location is pushed slightly up in frequency. A secondary peak typically also forms, which can be regarded as a secondary compensatory effect—when the main peak has been pushed up in frequency, a minimum forms on its right side to balance the mean spectral density in this ω range. Thus, the U-shaped band between the holon bounds is likely a spurious feature, which we demonstrate explicitly next.

It has been shown that a sharp edge followed by a continuum with power-law behavior (close to the edge) can be obtained in SAC when the distance $d_i = \omega_i - \omega_{i-1}$ is constrained to be monotonically increasing with i [51], as illustrated in Fig. 6(a). This constraint is associated with an entropic pressure forcing a divergent form (in the limit of a large number N_ω of δ -functions) $A(\omega) \sim (\omega - \langle \omega_1 \rangle)^{-1/2}$, where $\langle \omega_1 \rangle$, the edge location, is the mean

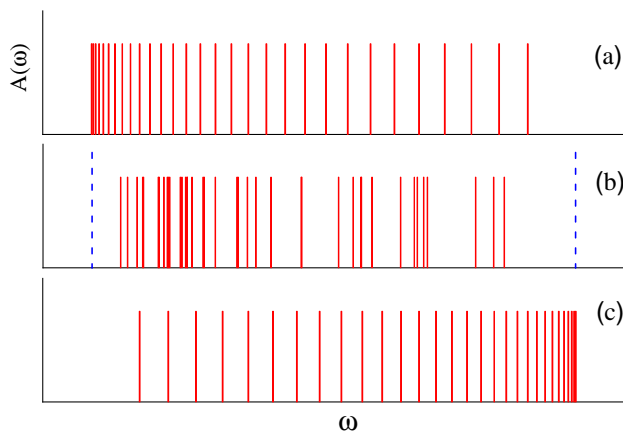


FIG. 6. Constraints on the sampled δ -functions that are combined in various ways here in constrained SAC. In (a) and (c), equal-weight δ -functions are constrained to monotonically changing spacing, increasing from the left to right in (a) and vice versa in (c); $\omega_i - \omega_{i-1} \leq \omega_{i+1} - \omega_i$ and $\omega_i - \omega_{i-1} \geq \omega_{i+1} - \omega_i$, respectively. In (b) the locations of otherwise unconstrained δ -functions are bounded from below by the edge in (a) or, for a two-edged spectrum, also from above by the edge in (c). The relative weights of the different components of the spectrum can be optimized by χ^2 minimization at fixed sampling temperature. The locations of all the δ -functions are sampled, including the edge(s).

of the energy of the lowest δ -function. The sampled edge location typically fluctuates very little once the process has equilibrated and ω_1 has reached a small optimal frequency window. Away from the immediate neighborhood of the edge, the spectrum can take any monotonically decaying form as dictated by the QMC data. In the case of the prototypical Heisenberg chain, the dynamic spin structure factor (which exhibits a spinon continuum with a divergent spectral weight at the lower edge) obtained this way compares very favorably with Bethe ansatz results [51]. To incorporate possible non-monotonic features above the edge, the constrained parametrization can be combined with another set of δ -functions, which are unconstrained except for the lowest frequency required to be above the edge ω_1 of the distance-monotonic set. The relative weight of the two sets can be optimized by minimizing the goodness of fit χ^2 at a fixed sampling temperature; see Ref. [51] for details.

Here we further extend this approach to also involve an upper edge, combining three different sets of mutually constrained δ -functions, as illustrated in Fig. 6. We will apply both the edge and double-edge constrained parametrizations next. While it is possible to optimize the relative weights of all three sets (two different weight ratios), in test cases we find that the spectrum does not change very much when the weights are of similar magnitude. This is because the unconstrained and constrained parts can adapt in many different ways to represent a near optimal weight distribution. Therefore, to avoid excessively time consuming optimizations of a large number

of spectra $A(k, \omega)$, we simply set the relative weight of all three sets to $1/3$ for most cases.

Results with the double edge are shown in Fig. 4(b) and examples of fixed- k profiles are shown in Fig. 5(b). Here the sharp bounds coincide very closely with the predicted edge singularities. The U-shaped broad band above the lower holon edge is now absent, confirming our suspicion that this feature was spurious and a consequence of the insufficient resolution of the lower edge in the unconstrained results in Fig. 4(a). The expected holon singularities inside the continuum are resolved as intermediate peaks at locations marked by circles in Fig. 4(b) that are typically close to their predicted singular holon edges. Note that the same color scale is used for all the heat maps in Fig. 4, which implies that the bright broadened bands close to the expected edge are not present in the constrained results, where the edges are tall but very thin—the fixed- k profiles in Fig. 5 are clearer in this regard.

Given that the spin-charge separation ansatz is not exact and multi-spinon excitations in principle should also exist, there is likely some small amount of spectral weight also above the upper singular edge. It is therefore also useful to consider only a constrained edge at the lower end of the spectrum. These results are shown in in Figs. 4(c) and 5(c). The lower edge does not move much relative to that in the double-edge results, but other features are more smeared out. The upper edge is still sharper than in the completely unconstrained results, as is the holon band away from the edges. The very small amount of weight above the location of the sharp upper bound in the double-edge results indicate that there is only very little weight there also in the true spectrum—even smaller than what is seen in 4(c), considering the broadening present in the SAC spectrum. The ED spectrum for $L = 28$ [25] also does not show substantial weight above the predicted upper edge.

We next consider the t - J chain at the supersymmetric point, with $t = 1$ and $J = 2$ (thus, the off-diagonal spin interaction and the kinetic energy have the same matrix elements), where the $k = 0$ single-hole spectral function is exactly a δ -function; $A(k = 0, \omega) = \delta(\omega - 2t)/2$ [8, 9, 12]. As seen in Fig. 7(a), the unconstrained SAC result is fully consistent with this form, with only a small broadening arising from the statistical errors in imaginary time. In Figs. 7(b) and 7(a), we have fitted $G(0, \tau)$ to a single δ -function, and adding other contributions does not improve the fit (a constrained parametrization that we will discuss in more detail in Sec. III B). Away from $k = 0$, in the supersymmetric model there is no separate lower spinon branch within the spin-charge separation ansatz if the bare dispersion parameters $t_h = 2t$ and $J_s = J$ are used, because then $k_0 = 0$. However, all three SAC parametrizations in Fig. 7 consistently show a flattening out of the lower edge of the spectrum both for $k \rightarrow 0$ and $k \rightarrow \pi$. The entire lower edge, except close to $k = \pi$, can be well accounted for if we use different phenomenologically spinon-holon parameters; here we only adjust the

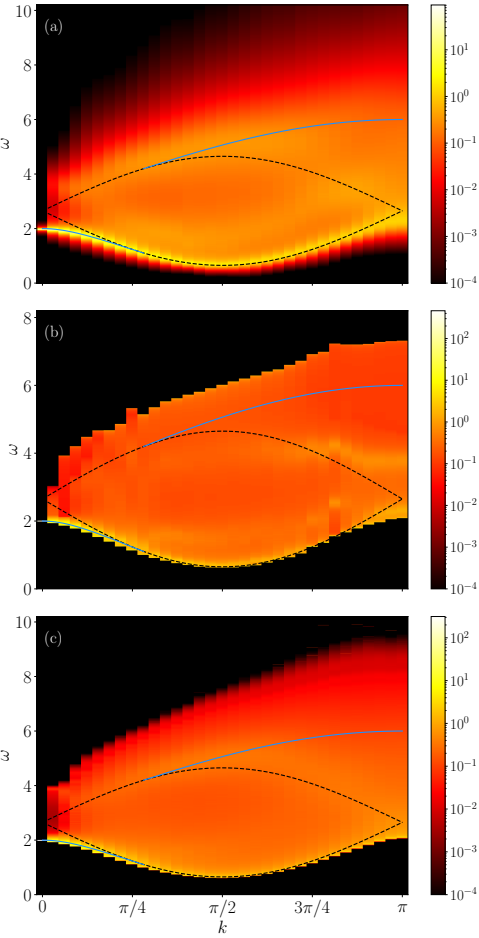


FIG. 7. Spectral function $A(k, \omega)$ of the t - J model at the supersymmetric point, $t = 1$, $J = 2$. The panels correspond to three different variants of SAC in the same way as in Fig. 4 and the curves show the predicted locations of the singularities with $J_s = 1.35$ and $t_h = 2$ in Eqs. (32), chosen to match the holon dispersion close to $k = \pi$ and the putative spinon branch close to $k = 0$.

spinon dispersion, with $J_s = 1.35$, and keep the holon dispersion at its bare form. The deviations at $k = \pi$ cast some doubt on the predictions of the spin-charge separation ansatz, as we will discuss further below.

Also in this case, with unconstrained SAC a likely spurious broad band is produced above the lower holon branch, which is seen more clearly in the $k = \pi/2$ profile in Fig. 5(d). With the double-edge constraint applied in Fig. 7(b), the predicted upper edge is not as well reproduced as in the previous $J/t = 0.4$ case in Fig. 4(b). Moreover, the dim band that may be spurious still appears within the predicted holon bounds. It is possible that the model with this rather large J/t value has more substantial high-energy spectral weight that is not captured by the spin-charge separation ansatz, which includes only one excited anti-spinon. The enforced upper edge would then be pushed up to partially include it, which is possible since the statistical information in

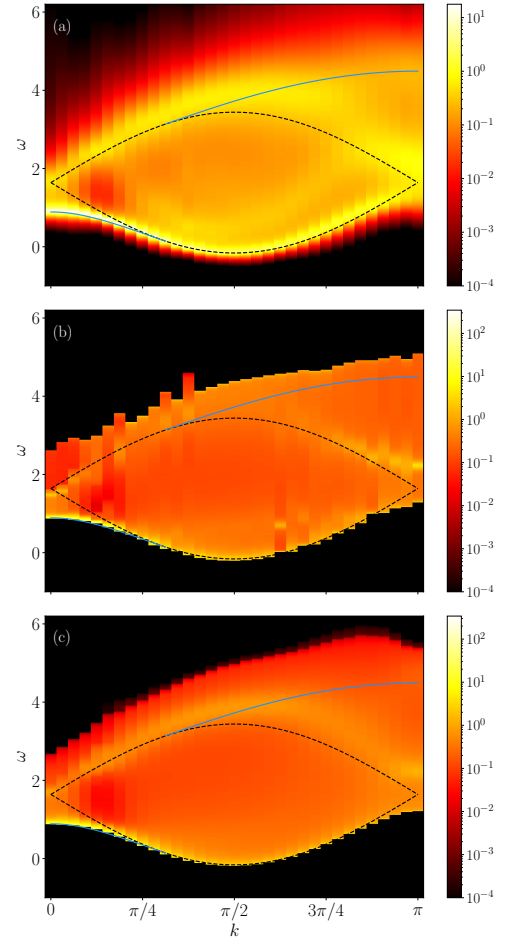


FIG. 8. Spectral function of the t - J - Q model at the dimerization transition; $t = 1$, $J = 1$, $Q = 0.1645$. The panels correspond to three different variants of SAC in the same way as in Figs. 4 and 7. The curves show the predicted locations of the singularities, with the holon hopping strength $t_h = 1.8$ chosen to optimize the agreement with the lower edge close to $k = \pi/2$. The constant in the spinon dispersion Eq. (32a) is set at $J_s = 1.05$ to match the lower edge (putative spinon branch) close to $k = 0$.

$G(k, \tau)$ is limited and SAC can produce good fits to the data even though the imposed behavior at the upper edge is not strictly correct. Indeed, when only the lower edge is imposed, Fig. 7(c) shows a dim broad upper holon band close to the predicted location, and there is no spurious band close to the lower edge. Spectral weight extends to higher ω than in Fig. 7(b), well above the predicted upper bound. The difference between the predicted and observed bound looks smaller in the case of $J = 0.4$, Fig. 4(c), for which the QMC data quality is very similar. Note, however, that the logarithmic heat map visually exaggerates regions of small but nonzero spectral weight, and the linear scales used in Fig. 5 are better suited for quantitative judgment.

Turning on the Q interaction, in Fig. 8, as well as Figs. 5(g)-5(i), results are shown for the three different

SAC parametrizations in the case where Q/J is set to the critical value of the dimerization transition of the host, where the marginal operator driving the transition vanishes. Here we have set the holon coefficient to $t_h = 1.8$ so as to best reproduce the lower bound close to the minimum at $k = \pi/2$. For the spinon dispersion, we set $J_s = 1.05$ to reproduce the flattened-out edge close to $k = 0$ in terms of a putative spinon band. Similar to the supersymmetric point, there are clear deviations from the predicted holon lower bound close to $k = \pi$; here these deviations are even more pronounced. Overall, the results do not differ much qualitatively from those for $Q = 0$, which would also not be expected as the host spin system is still in the same type of critical ground state, only without the marginal operator inducing logarithmic corrections.

Let us now return to the unexplained deviations from the predicted cosine form of the holon dispersion close to $k = \pi$ in both Fig. 7 and Fig. 8. These deviations also cast some doubt on the matching of the edge close to $k = 0$ by adjusting the phenomenological dispersion parameters. It appears that the width of the holon spectrum does not shrink to a point as $k \rightarrow 0$ and $k \rightarrow \pi$ in the manner predicted. This behavior might actually be expected in light of the fact that all states excited by the fermion destruction operator have the same quantum numbers. Thus, the level crossings of holon energies (in the extended BZ) when the predicted upper and lower holon bounds come together at $k = 0$ and $k = \pi$ should be avoided level crossings, with a gap forming. In principle such a gap may shrink to zero with increasing system size, which we do not observe. The lower bound with its flattening out for $k \rightarrow 0$ and $k \rightarrow \pi$ is only very weakly dependent on the system size for $L \geq 32$. The finite gap in the thermodynamic limit suggests the importance of interactions not included in the spin-charge separation ansatz. The use of the ansatz to fit a lower spinon branch in Figs. 7 and 8 may then not be correct and it is possible that the lower edge always corresponds to the holon dispersion in these cases and that a separate spinon branch only forms for small J/t in the t - J model, and for also small Q/t in the t - J - Q model.

B. Spontaneously dimerized phase

For $(Q/J) > (Q/J)_c \approx 0.1645$ the J - Q chain is spontaneously dimerized [59, 78], i.e., with a two-fold degenerate ground state, $|A\rangle$ and $|B\rangle$, in the thermodynamic limit. Here spinons represent domain walls between $|A\rangle$ and $|B\rangle$ ordered chain segments and they are also deconfined. It is not a priori clear whether residual interactions could cause binding of a holon and a spinon into a spin polaron, however. We illustrate this question in Fig. 9, where the injection of a hole into a dimerized chain leads to the replacement of a singlet by a hole and a spinon. The spinon-holon pair can propagate without separating, but once the partons do separate they may in principle

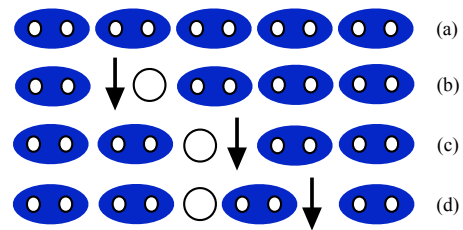


FIG. 9. Illustration of a single hole injected into the VBS phase (a), where blue ovals correspond to singlets. In (b) the resulting holon is accompanied by a neighboring unpaired spin. The tightly bound spinon-holon object (spin-polaron) in can hop by quantum fluctuations and leave the VBS pattern in the same phase A, exemplified in (c). The spinon and holon can also separate, as in (d), thereby creating a segment of singlets forming a translated VBS pattern B in between. Such states may either evolve to become fully spin-charge separated or contain extended spinon-holon bound states as discussed in the text.

move further away and deconfine without additional energy cost. However, if there is a residual attractive interaction, one or several bound states should form. The binding forces here include the loss of negative kinetic energy that allow the spinon and holon to resonate on a single bond without moving. In an extreme case of a localized spin polaron surrounded by unbreakable singlets, the ground state energy of the spinon-holon (in the even state with respect to spinon-holon permutation) is $-t$, with the corresponding internal excited state (odd with respect to permutation) is $+t$. The cost of breaking up the pair is therefore $2t$, though this cost is compensated by the kinetic energy of the deconfined partons and by the different effective spin-spin interactions in the neighborhood of the spinon and holon. Deconfined states will definitely exist at sufficiently high energy, but it is possible that at least the lowest state could be a spin polaron for some momenta, which would be manifested in $A(k, \omega)$ as an isolated δ function at energy ω_k .

Before addressing the possibility of a spin polaron quasiparticle, in Fig. 10 we present results for $A(k, \omega)$ at $t = Q = 1$, $J = 0$, i.e., deep inside the VBS phase, using the same three SAC parametrizations as in Sec. III A. While at first sight the results look very similar to the previous cases with the critical host state, there are some notable differences. In particular, the band previously categorized as the upper holon band is much more prominent, and there is also more spectral weight above it. There is no sign of separate spinon and holon bands at small k and the band width here is large compared to the previous cases. For k close to π , the shape of the spectral weight distribution is also different from previous cases, narrowing on approach to $k = \pi$ instead of exhibiting the increase in the upper band energy that was due to the spinon branch in the previous cases. In the scenario of a spin polaron as the lowest excitation, the bright second band in the middle of the continuum, which is particularly prominent in Fig. 10(c), is inter-

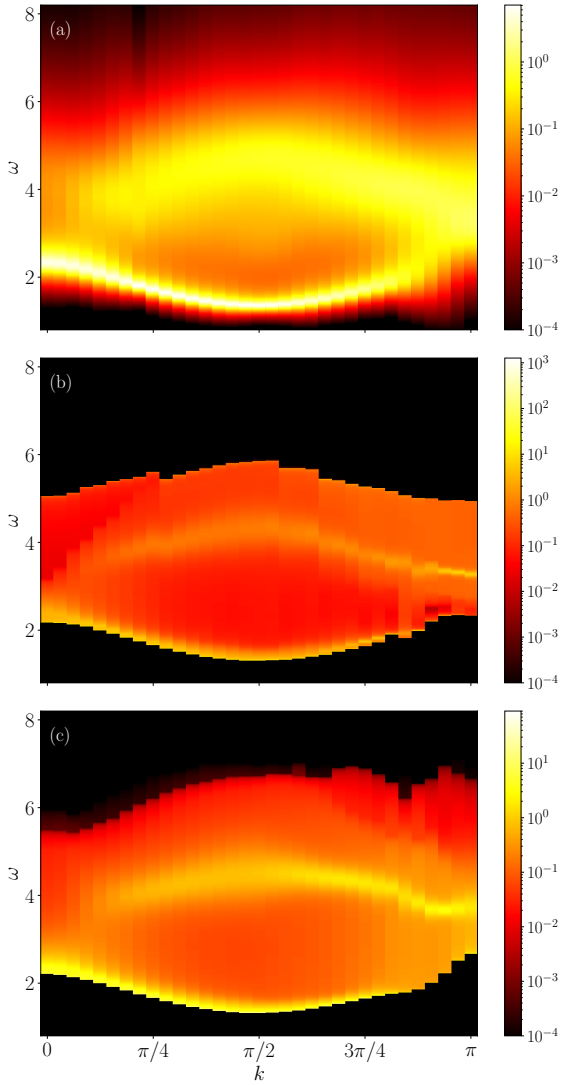


FIG. 10. Spectral function of the t - J - Q model in the dimerized phase, with $t = 1$, $J = 0$, $Q = 1$. The SAC parametrizations are the same as in the previous 3-panel graphs.

preted as the permutation-odd spin polaron, while the lower edge corresponds to the permutation even case.

To further investigate the spin polaron scenario, we adopt the SAC parametrization first introduced in Ref. [50] and illustrated in Fig. 11, where a sharp quasiparticle at the lower edge of the spectrum is represented by a single “macroscopic” δ -function holding a fraction a_0 of the total spectral followed by a continuum represented by a large number N_ω of equal-weight, $a_i = (1 - a_0)/N_\omega$, δ -functions above ω_0 . The quasi-particle frequency ω_0 is sampled at constant a_0 along with all $\omega_{i>0}$. Once the sampling has equilibrated, ω_0 is essentially fixed (unless a_0 is very small). The parameter quasiparticle weight is determined by optimizing the goodness-of-fit χ^2 in a scan over a range of a_0 values. Using this approach we obtain the momentum dependent spectral function and optimal quasiparticle weight $a_0(k)$ shown in Fig. 12. Notably, the

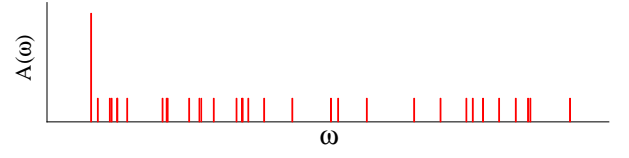


FIG. 11. Parametrization of a spectral function with a sharp quasiparticle edge modeled by a macroscopic δ -function with relative weight a_0 , with its location ω_0 being the lower bound for a large number of equal-amplitude microscopic δ -functions representing a continuum with weight $1 - a_0$. The optimal value of a_0 is determined by a scan to find the best statistical match of the sampled average to the QMC data.

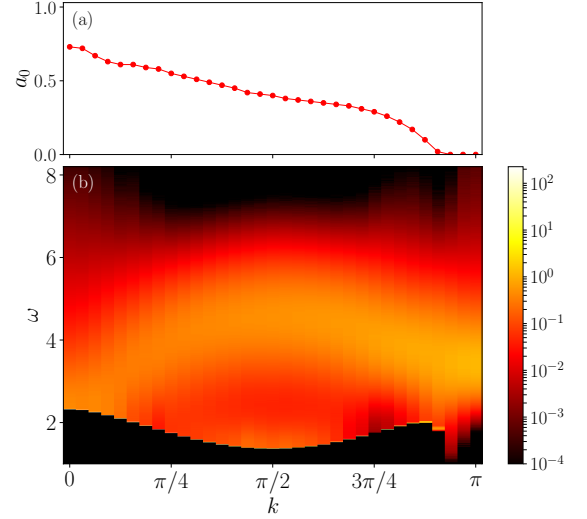


FIG. 12. Spectral function of the t - J - Q model with $t = 1$, $J = 0$, and $Q = 1$, using the parametrization with δ -function edge in in Fig. 11. The quasiparticle weight $a_0(k)$ is shown in (a). The heat map of $A(k, \omega)$ in (b) shows the contributions above the edge, with relative weight $1 - a_0(k)$. The small weight $a_0(k)$ close to $k = \pi$ makes the lower edge of the spectrum difficult to determine there, as reflected in the significant scatter.

quasiparticle weight is large close to $k = 0$ and drops to zero in the neighborhood of $k = \pi$, in the latter case causing large uncertainties in the actual location of the edge. The very small spectral weight at low energy for $k \approx \pi$ is also seen with the power-law edge parametrizations in Figs. 10(b) and 10(c). There is also no sign of a spinon branch, neither at the lower as close to $k = 0$ or the upper bound of the spectrum close to $k = \pi$.

We do not detect any signs of a gap between the potential spin polaron and the continuum of excitations, though a very small gap cannot be excluded. With the unconstrained sampling above the δ -edge, it is not possible to resolve a very small gap because of entropic pressures that tend to spread out the continuum while maintaining a good fit to the QMC data. To explore the possibility of a very small gap separating an isolated sharp quasiparticle from the continuum, we impose a further

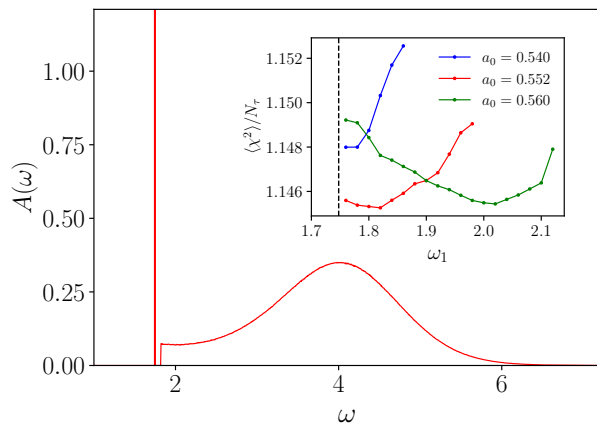


FIG. 13. Example of an optimized second gap with the same QMC data as in Fig. 12 at $k = \pi/4$. The inset shows the goodness of fit versus the second gap ω_1 for three values of the weight a_0 of the edge δ -function. The optimal parameters on the grid used are $a_0 = 0.552$ and $\omega_1 = 1.82$, and the vertical dashed line is the position of the lower bound ω_0 .

constraint; a lower bound $\omega_1 > \omega_0$ for the contributions above the macroscopic δ -function at ω_0 . Here ω_0 is again sampled but fluctuates very little, and ω_1 is optimized along with the weight a_0 . To implement this optimization, we perform a scan over ω_1 for several different values a_0 , searching for the optimal pair (a_0, ω_1) corresponding to the χ^2 minimum. This optimization in a 2D parameter space is time consuming but helped by the fact that a_0 obtained without the additional constraint is already very close to the further refined value. See Fig. 13 for a simple illustration where we demonstrate three ω_1 scans and the corresponding optimal $A(\omega)$.

Using the second-gap approach, the optimized gaps obtained with the data in Fig. 12 (in cases where the weight a_0 is not close to 0) are very small. The case of $k = \pi/4$ is shown in Fig. 13. The fact that the gap is small and the spectral weight is not piling up close to the ω_1 edge gives further support to the existence of a spin polaron—a single isolated bound state followed by a continuum of excitations that may arise from long-lived larger spinon-holon states whose broad peaks merge into a continuum. There should still also be a high-energy continuum of fractionalized excitations.

While it is not possible to conclusively determine the nature of the low-energy excitations in this case based on the results presented, the differences with respect to the known spin-charge separated cases in Sec. III A make us lean toward the spin polaron scenario. The presence of at least one bound state has also previously been found in the frustrated J_1 - J_2 Heisenberg chain at the special point $J_2/J_1 = 1/2$ where the ground state is an exact dimer-singlet state [79–82]. The analogy with this case also strengthens the case for bound states in the spontaneously dimerized t - J - Q chain.

The lowest edge with quasi-particle peak should cor-

respond to the even (with respect to permutation of the partons) spin-polaron and the broad band at higher energy in Fig. 12 would be the odd state, dressed by multi-spinon excitations causing broadening. The separation between the even and odd cases should be expected to be of order $2t = 2$, but is somewhat larger when maximized at $k = \pi/2$ in the results presented here.

IV. SPIN POLARONS IN BOND-ALTERNATING CHAINS

To further investigate spin polarons in 1D systems, we consider the t - J chain with alternating strong (t_1, J_1) and weak (t_2, J_2) bond parameters. In the limit where $t_1, J_1 \gg t_2, J_2$ and $t_i \ll J_i$, an inserted hole strongly binds to a neighboring spin on a strong bond to form a localized spin polaron. Here the sketch in Fig. 9(a) still applies, with the shown pattern assumed to be the one minimizing the energy, e.g., the singlets reside on the strong bonds. When inserting a hole, the accompanying unpaired spin will then also reside on the same bond, where the singlet was broken. In this case there is no doubt that a bound state forms, and this spin polaron will move with an effective hopping $\propto t_2^2/J_1$ between the strong bonds, corresponding to Figs. 9(b) and 9(c). The spin polaron has two internal degrees of freedom; hence there will be even and odd bands separated by a gap $\propto t_1$ (note, however, that there are corresponding completely conserved quantum numbers only at special momenta, as we will discuss further below). The partons can still separate, as in Fig. 9(d), but in this case a string (in an analogy with a pair of quarks bound by a gluon string) of high-energy singlets form between them, unlike the VBS phase where the couplings are uniform. Thus, we expect a spectrum of some equally spaced even-odd pairs of levels. At high energies the string should become increasingly unstable; thus the life time of the bound state should become shorter and the corresponding spectral features broader.

To demonstrate this scenario explicitly, we first examine exact diagonalization (ED) results for $A(k, \omega)$ with parameters $t_1 = 0.8$, $J_1 = 6$, $t_2 = 0.1$, $J_2 = 1$. Here we aim for a large number of low-energy levels and use full diagonalization for $L = 12$, which is already sufficiently large for our purposes here. To present the results, we take the momentum from the unfolded BZ, i.e., that of the uniform chain, which makes it easier to analyze different bands of excitations. Results for the energy levels versus momentum are shown in Fig. 14(a), where the lines are colored according to the squared matrix elements in the definition Eq. (24) of the spectral function, using a logarithmic scale. The separation between the lowest two levels is roughly $2t_1$ and the bands are only weakly dispersive on this scale, in agreement with the above reasoning.

A noteworthy feature is that the quasiparticle weight of the lowest band vanishes at $k = \pi$, while the second band

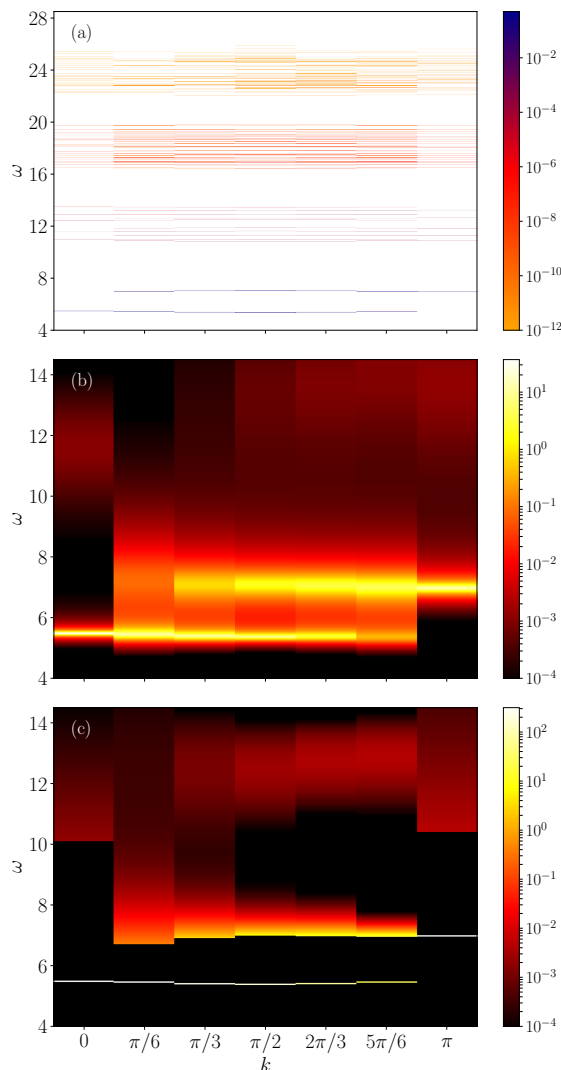


FIG. 14. Single-hole spectral function $A(k, \omega)$ of the bond-alternating t_1 - J_1 - t_2 - J_2 chain of length $L = 12$ with $t_1 = 0.8$, $J_1 = 6$, $t_2 = 0.1$, $J_2 = 1$. (a) is based on full exact diagonalization, with the colors corresponding to the amplitudes of the δ -functions in Eq. (24). The other panels show corresponding SAC results, with (b) from unconstrained sampling and (c) with a macroscopic δ -function as the lower edge and an optimized gap to the other contributions, i.e., sampling with the parametrization in Fig. 11 but with an additional optimized constraint on the allowed space for the “microscopic” δ functions above the edge. Note that the color scale in (a) is inverted (darker colors for larger spectral weights), to more clearly show the levels at the lowest energies.

shows no weight at $k = 0$, even though the corresponding states do exist in the spectrum. This behavior is consistent with the odd versus even internal permutation symmetry of the partons of the spin polaron by the following arguments: $c_{k=0, \uparrow}$ creates an odd polaron when acting on the singlet product state illustrated in Fig. 9(a), thus with no overlap with the even state. Conversely $c_{k=\pi, \uparrow}$ creates an even polaron with no overlap with the odd

one. Since the sign structure of the spin wave function (the Marshall sign rule) is maintained even if Fig. 9(a) is not the exact ground state, the arguments remain valid also when $c_{0, \uparrow}$ and $c_{\pi, \uparrow}$ act on the true ground state of the spin model. Beyond these special cases, the even and odd branches are not associated with a conservation law, but the internal parity of the spin polaron can still be long-lived and lead to the observed band formation.

The lowest level pair is separated from the next group of levels in Fig. 14(a) (approximately in the frequency window $\omega = 10 \sim 14$) by a gap consistent with the J_1 scale. This group corresponds to the second even and odd bound states, with emergent broadening of these excitations corresponding to a finite life time of the higher bound states. Groups of levels at still higher energy are also broadened to an increasing extent and the even and odd parts of the bands become difficult to distinguish. The separation between the bands is roughly constant in accord with the linear potential of the string of mismatched singlets between the spinon and holon. While the lowest spin polaron can be expected to remain a sharp excitation with a single δ -function peak in $A(k, \omega)$, the sharp second band in Fig. 14(a) is likely a finite-size effect. For some model parameters and momenta, the second level indeed splits into two already for $L = 12$. On increasing the excitation energy, the string of dimerization mismatches will eventually break, which is facilitated by the creation of an additional spinon pair and subsequent recombination of one spinon with the holon. The broadening, and loss of probability amplitude, of the higher bands in Fig. 14(a) reflect the short life time of the longer strings and the low probability of creating large bound states by hole injection.

Unconstrained SAC results for the same system is shown in Fig. 14(b). The two lowest bands are resolved clearly, though of course with some broadening. The spectral weight of the higher bands is very small and only a dim broad peak is resolved in the approximate range of the second set of excitations around $\omega \approx 12$. When using the parametrization with optimized macroscopic δ -function edge, the dispersion relation of the lowest band is well reproduced but there is still a small spectral weight between it and the second band. As shown in Fig. 14(c), we can completely separate the two lowest bands by imposing the second-gap constraint $\omega_1 > \omega_0$ for the contributions above the macroscopic δ -function at ω_0 . Comparing with the ED results in Fig. 14(a), $\omega_0(k)$ and $\omega_1(k)$ of the two lowest band are very well reproduced in Fig. 14(c); within the same output bin width ($\Delta_\omega = 0.005$) from SAC for $\omega_0(k)$ and to within at most $\sim 4\%$ for $\omega_1(k)$ for all k .

Extending to larger system sizes with QMC and SAC, we observe overall similar features, as shown in Fig. 15 for the same parameter set as above but now for chain length $L = 64$. Unconstrained SAC again reveals two narrow bands close to those for $L = 12$ but with more clearly visible gradual fading of the spectral weight for the lower band when $k \rightarrow \pi$ and for the second band

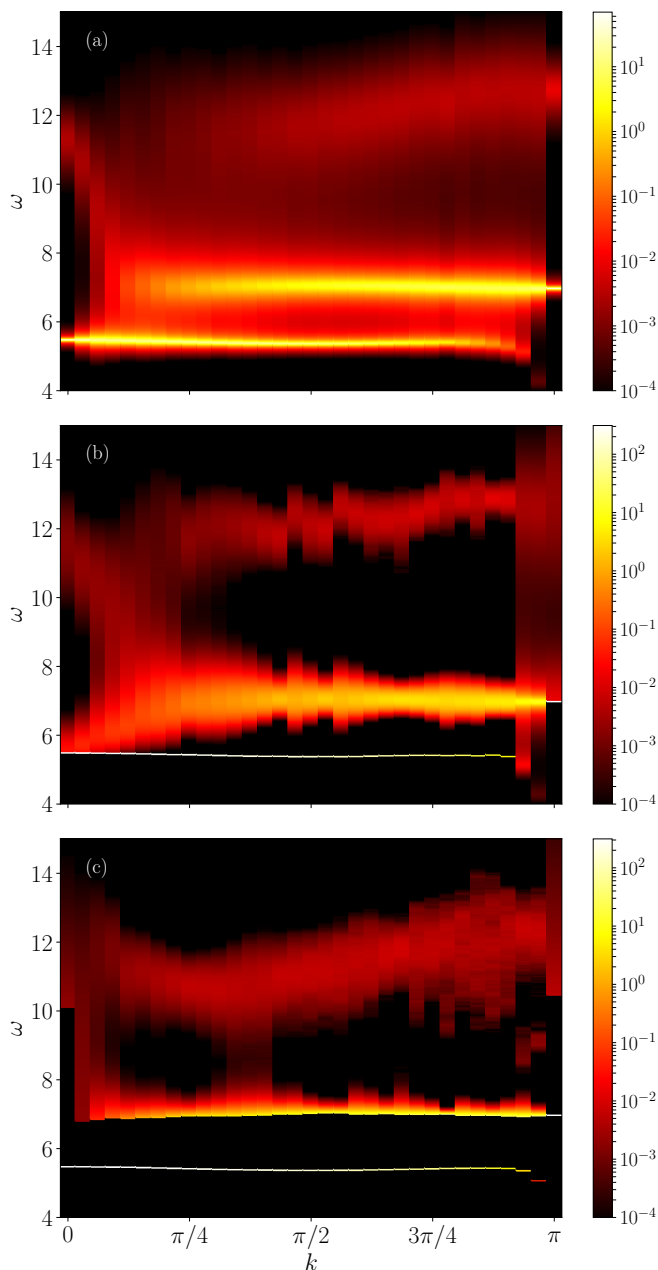


FIG. 15. Single-hole spectral function of the same model as in Fig. 14 but for system size $L = 64$. Three different SAC parametrizations are used as follows: (a) unconstrained with variable amplitudes, (b) single- δ quasiparticle edge (c) as in (b) but with an optimized lower bound for the contributions above the first quasiparticle.

when $k \rightarrow 0$. The third band is better defined than in the $L = 12$ unconstrained SAC results in Fig. 15(a) and is also more dispersive. In Fig. 15(b), where the δ -edge parametrization was used, the second band is better separated from the now sharp lower band, except in the neighborhood of $k = 0$ and $k = \pi$ —in the latter case the very small spectral weight makes it difficult to determine the optimal a_0 value.

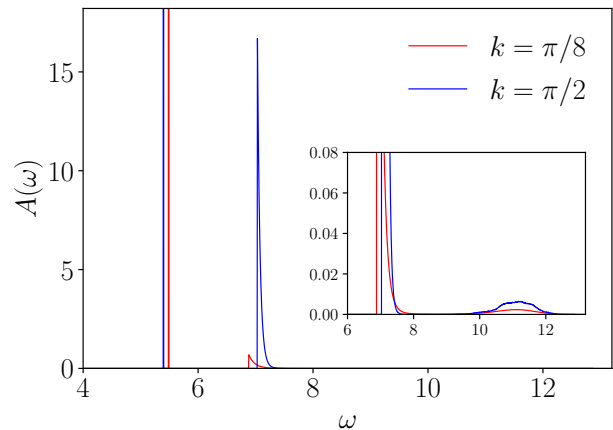


FIG. 16. Two representative vertical cuts of Fig. 15(c), at $k = \pi/8$ and $k = \pi/2$. The amplitude $a_0(k)$ of the lower δ -function was optimized along with the second gap $\omega_1(k)$ at which an asymmetric edge forms. The inset is zoomed in on the ω_1 edges and the small humps located at $\omega(k) = 10 \sim 12$.

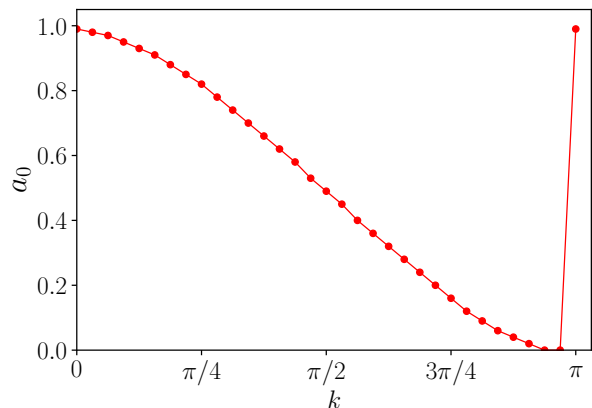


FIG. 17. Quasi-particle weight a_0 corresponding to Fig. 15(c). The jump at $k = \pi$ reflects vanishing a_0 of the first band at this momentum and the method then identifies the quasiparticle of the second band.

Further improving the results by optimizing the second gap $\omega_1(k)$, Fig. 15(c) also shows a rather sharp second band. The distance between the lowest bands is again close to $2t_1$ as expected for the odd and even spin polarons at this large modulation of the couplings. An interesting feature is that the third band (which likely involves merged even and odd sub-bands) now has a minimum between $k = \pi/4$ and $\pi/2$, different for the almost dispersionless band found above with ED for $L = 12$. There is very little spectral weight in a continuum at higher energies, reflecting the higher bound states that cannot be resolved. Fig. 16 shows the spectra at two values of k versus ω to further demonstrate the capability of the method with a second gap to resolve the two lowest bands and also likely give a good approximation of the third band. The quasiparticle weight a_0 is shown versus k in Fig. 17 based on the results in Fig. 15(c). The

a_0 values from Figs. 15(a) and 15(b) are very similar to those graphed. Note that the jump at $k = \pi$ reflects the absence of weight in the lower band at this momentum, and the method then instead finds the δ -edge in the second band. Since the spectral weight beyond the two lowest bands is very small, the relative weight $a_1(k)$ of the second band is very close to $1 - a_0(k)$; thus spectral weight is gradually transferred from the odd to the even spin polaron as k changes from 0 to π .

V. SUMMARY AND DISCUSSION

We have systematically investigated the fermionic single-hole spectral function $A(k, \omega)$ of $S = 1/2$ quantum spin chains with different types of ground states. Our main aim here has been to test the capabilities of constrained SAC to resolve sharp edge features that typically cannot be reproduced with conventional analytic continuation methods—here exemplified by unconstrained SAC but the maximum-entropy method [46] also has very similar limitations. One may argue that the constraints introduce bias and the approach either just confirms previously known facts or produces misleading results. The reality, however, is that sharp features cannot be resolved unless some corresponding information is provided, and the imposed constraints improve the ability of SAC (or other methods where similar constraints could be implemented) to deliver reliable dispersion relations for the lowest excitations, reduce the presence of spurious features at higher energy, and better resolve actual features above the edge. Thus, when the existence of a sharp edge is known, its incorporation as a constraint can be of great value. Note that the default models used in the maximum-entropy method could also in principle be optimized in a way analogous to the constraints in SAC (see Ref. [51] for further discussion) but SAC often represents a more natural framework in this regard.

Here we have used both a lower edge with a sharp δ -function and one corresponding to a divergent continuum, in one case also using such an edge at the upper bound of the spectrum. We also demonstrated that a δ -function with a second excitation gap followed by and the edge is useful for resolving second gaps. In cases

where the exact nature of the edge is not known, it is useful to compare different constraints. Here we have only provided visual comparisons, but in principle statistical cross-validation methods can also be used to single out the most likely spectrum out of a group [54].

As for results, in the case of the conventional t - J chain and t - J - Q chain with Q/J inside the same critical phase of the host system, the incorporation of power-law divergent edges produced spectral functions with some features closely matching the spin-charge separation ansatz. However, in some cases we also pointed out that the holon dispersion relation exhibits gaps between the upper and lower bounds at the point where the two should merge (cross each other in momentum space) according to the ansatz. This manifestation of the approximate nature of the ansatz motivates further study of spin-charge separation with more sophisticated analytical methods. With large Q/J , inside the spontaneously dimerized phase, our results point to an isolated spin polaron bound state as the lowest excitation. This state should be even with respect to parton permutation and we also detected a higher band consistent with odd-parity polarons with finite life time. In the statically dimerized chain, we were likewise able to resolve multiple band of spin polarons.

Overall, our results demonstrate the effectiveness of constrained SAC approaches in reproducing spectral functions with sharp features that are beyond the resolution of other numerical methods. In combination with large-scale quantum Monte Carlo simulations, these SAC methods highlight the potential for much broader applications to a wide range of quantum many-body systems. Results for the quantum-critical 2D t - J - Q are reported in Ref. [58].

ACKNOWLEDGMENTS

We would like to thank Karlo Penc and Qimiao Si for discussions. This research was supported by the Simons Foundation under Grant No. 511064. The numerical calculations were carried out on the Shared Computing Cluster managed by Boston University's Research Computing Services.

-
- [1] Y. Hasegawa and D. Poilblanc, Hole dynamics in the t-J model: An exact diagonalization study, *Phys. Rev. B* **40**, 9035 (1989).
 - [2] E. Dagotto, R. Joynt, A. Moreo, S. Bacci, and E. Gagliano, Strongly correlated electronic systems with one hole: Dynamical properties, *Phys. Rev. B* **41**, 9049 (1990).
 - [3] E. Dagotto, A. Moreo, F. Ortolani, D. Poilblanc, and J. Riera, Static and dynamical properties of doped Hubbard clusters, *Phys. Rev. B* **45**, 10741 (1992).
 - [4] D. Poilblanc, T. Ziman, H. J. Schulz, and E. Dagotto, Dynamical properties of a single hole in an antiferromagnet, *Phys. Rev. B* **47**, 14267 (1993).
 - [5] D. Poilblanc, H. J. Schulz, and T. Ziman, Single-hole spectral density in an antiferromagnetic background, *Phys. Rev. B* **47**, 3268 (1993).
 - [6] R. Preuss, A. Muramatsu, W. von der Linden, P. Dieterich, F. F. Assaad, and W. Hanke, Spectral Properties of the One-Dimensional Hubbard Model, *Phys. Rev. Lett.* **73**, 732 (1994).
 - [7] P. Béran, D. Poilblanc, and R. Laughlin, Evidence for composite nature of quasiparticles in the 2D t-J model,

- Nuclear Physics B* **473**, 707 (1996).
- [8] S. Sorella, Sharp photoemission spectra in the quantum antiferromagnet, *Phys. Rev. B* **53**, 15119 (1996).
- [9] S. Sorella and A. Parola, Spectral Properties of One Dimensional Insulators and Superconductors, *Phys. Rev. Lett.* **76**, 4604 (1996).
- [10] H. Suzuura and N. Nagaosa, Spin-charge separation in angle-resolved photoemission spectra, *Phys. Rev. B* **56**, 3548 (1997).
- [11] K. Penc, K. Hallberg, F. Mila, and H. Shiba, Spectral functions of the one-dimensional Hubbard model in the $U \rightarrow +\infty$ limit: How to use the factorized wave function, *Phys. Rev. B* **55**, 15475 (1997).
- [12] S. Sorella and A. Parola, Theory of hole propagation in one-dimensional insulators and superconductors, *Phys. Rev. B* **57**, 6444 (1998).
- [13] G. B. Martins, C. Gazza, J. C. Xavier, A. Feiguin, and E. Dagotto, Doped Stripes in Models for the Cuprates Emerging from the One-Hole Properties of the Insulator, *Phys. Rev. Lett.* **84**, 5844 (2000).
- [14] S. Capponi and F. F. Assaad, Spin and charge dynamics of the ferromagnetic and antiferromagnetic two-dimensional half-filled Kondo lattice model, *Phys. Rev. B* **63**, 155114 (2001).
- [15] K. A. Al-Hassanieh, F. A. Reboredo, A. E. Feiguin, I. González, and E. Dagotto, Excitons in the One-Dimensional Hubbard Model: A Real-Time Study, *Phys. Rev. Lett.* **100**, 166403 (2008).
- [16] T. A. Maier, D. Poilblanc, and D. J. Scalapino, Dynamics of the Pairing Interaction in the Hubbard and $t-J$ Models of High-Temperature Superconductors, *Phys. Rev. Lett.* **100**, 237001 (2008).
- [17] E. H. Lieb and F. Y. Wu, Absence of Mott Transition in an Exact Solution of the Short-Range, One-Band Model in One Dimension, *Phys. Rev. Lett.* **20**, 1445 (1968).
- [18] J. Voit, One-dimensional Fermi liquids, *Reports on Progress in Physics* **58**, 977 (1995).
- [19] M. Arikawa, Y. Saiga, and Y. Kuramoto, Electron Addition Spectrum in the Supersymmetric $t-J$ Model with Inverse-Square Interaction, *Phys. Rev. Lett.* **86**, 3096 (2001).
- [20] M. Arikawa, T. Yamamoto, Y. Saiga, and Y. Kuramoto, Exact electron addition spectrum in 1D supersymmetric $t-J$ model with $1/r^2$ interaction, *Nuclear Physics B* **702**, 380 (2004).
- [21] C. Kollath, U. Schollwöck, and W. Zwerger, Spin-Charge Separation in Cold Fermi Gases: A Real Time Analysis, *Phys. Rev. Lett.* **95**, 176401 (2005).
- [22] C. Kollath and U. Schollwöck, Cold Fermi gases: a new perspective on spin-charge separation, *New Journal of Physics* **8**, 220 (2006).
- [23] D. Poilblanc, A. Läuchli, M. Mambrini, and F. Mila, Spinon deconfinement in doped frustrated quantum antiferromagnets, *Phys. Rev. B* **73**, 100403 (2006).
- [24] J. Šmakov, A. L. Chernyshev, and S. R. White, Spinon-holon interactions in an anisotropic $t-J$ chain: A comprehensive study, *Phys. Rev. B* **76**, 115106 (2007).
- [25] P. Wrzosek, A. Kłosiński, Y. Wang, M. Berciu, C. E. Agrapides, and K. Wohlfeld, The fate of the spin polaron in the 1D antiferromagnets, *SciPost Phys.* **17**, 018 (2024).
- [26] C. Kim, A. Y. Matsuura, Z.-X. Shen, N. Motoyama, H. Eisaki, S. Uchida, T. Tohyama, and S. Maekawa, Observation of Spin-Charge Separation in One-Dimensional SrCuO₂, *Phys. Rev. Lett.* **77**, 4054 (1996).
- [27] C. Kim, Z.-X. Shen, N. Motoyama, H. Eisaki, S. Uchida, T. Tohyama, and S. Maekawa, Separation of spin and charge excitations in one-dimensional SrCuO₂, *Phys. Rev. B* **56**, 15589 (1997).
- [28] H. Fujisawa, T. Yokoya, T. Takahashi, S. Miyasaka, M. Kibune, and H. Takagi, Angle-resolved photoemission study of Sr₂CuO₃, *Phys. Rev. B* **59**, 7358 (1999).
- [29] A. Recati, P. O. Fedichev, W. Zwerger, and P. Zoller, Spin-Charge Separation in Ultracold Quantum Gases, *Phys. Rev. Lett.* **90**, 020401 (2003).
- [30] A. Koitzsch, S. V. Borisenko, J. Geck, V. B. Zabolotnyy, M. Knupfer, J. Fink, P. Ribeiro, B. Büchner, and R. Follath, Current spinon-holon description of the one-dimensional charge-transfer insulator SrCuO₂: Angle-resolved photoemission measurements, *Phys. Rev. B* **73**, 201101 (2006).
- [31] B. J. Kim, H. Koh, E. Rotenberg, S. J. Oh, H. Eisaki, N. Motoyama, S. Uchida, T. Tohyama, S. Maekawa, Z. X. Shen, and C. Kim, Distinct spinon and holon dispersions in photoemission spectral functions from one-dimensional SrCuO₂, *Nature Physics* **2**, 397 (2006).
- [32] J. Vijayan, P. Sompet, G. Salomon, J. Koepsell, S. Hirthe, A. Bohrdt, F. Grusdt, I. Bloch, and C. Gross, Time-resolved observation of spin-charge deconfinement in fermionic Hubbard chains, *Science* **367**, 186 (2020).
- [33] J. G. Bednorz and K. A. Müller, Possible high T_c superconductivity in the Ba-La-Cu-O system, *Z. Phys. B: Condens. Matter* **64**, 189 (1986).
- [34] S. A. Trugman, Interaction of holes in a Hubbard antiferromagnet and high-temperature superconductivity, *Phys. Rev. B* **37**, 1597 (1988).
- [35] C. L. Kane, P. A. Lee, and N. Read, Motion of a single hole in a quantum antiferromagnet, *Phys. Rev. B* **39**, 6880 (1989).
- [36] G. Martinez and P. Horsch, Spin polarons in the t - J model, *Phys. Rev. B* **44**, 317 (1991).
- [37] S. R. White, Density matrix formulation for quantum renormalization groups, *Phys. Rev. Lett.* **69**, 2863 (1992).
- [38] S. R. White, Density-matrix algorithms for quantum renormalization groups, *Phys. Rev. B* **48**, 10345 (1993).
- [39] S. Östlund and S. Rommer, Thermodynamic Limit of Density Matrix Renormalization, *Phys. Rev. Lett.* **75**, 3537 (1995).
- [40] U. Schollwöck, The density-matrix renormalization group, *Rev. Mod. Phys.* **77**, 259 (2005).
- [41] U. Schollwöck, The density-matrix renormalization group in the age of matrix product states, *Annals of Physics* **326**, 96 (2011), January 2011 Special Issue.
- [42] L. Yang and A. E. Feiguin, From deconfined spinons to coherent magnons in an antiferromagnetic Heisenberg chain with long range interactions, *SciPost Phys.* **10**, 110 (2021).
- [43] L. Yang, I. Hamad, L. O. Manuel, and A. E. Feiguin, Fate of pairing and spin-charge separation in the presence of long-range antiferromagnetism, *Phys. Rev. B* **105**, 195104 (2022).
- [44] S.-H. Lin, M. P. Zaletel, and F. Pollmann, Efficient simulation of dynamics in two-dimensional quantum spin systems with isometric tensor networks, *Phys. Rev. B* **106**, 245102 (2022).
- [45] M. Drescher, L. Vanderstraeten, R. Moessner, and F. Pollmann, Dynamical signatures of symmetry-broken and liquid phases in an $S = \frac{1}{2}$ Heisenberg antiferromag-

- net on the triangular lattice, *Phys. Rev. B* **108**, L220401 (2023).
- [46] M. Jarrell and J. Gubernatis, Bayesian inference and the analytic continuation of imaginary-time quantum Monte Carlo data, *Physics Reports* **269**, 133 (1996).
- [47] A. W. Sandvik, Stochastic method for analytic continuation of quantum Monte Carlo data, *Phys. Rev. B* **57**, 10287 (1998).
- [48] K. S. D. Beach, Identifying the maximum entropy method as a special limit of stochastic analytic continuation (2004), [arXiv:cond-mat/0403055](https://arxiv.org/abs/cond-mat/0403055).
- [49] A. W. Sandvik, Constrained sampling method for analytic continuation, *Phys. Rev. E* **94**, 063308 (2016).
- [50] H. Shao, Y. Q. Qin, S. Capponi, S. Chesi, Z. Y. Meng, and A. W. Sandvik, Nearly Deconfined Spinon Excitations in the Square-Lattice Spin-1/2 Heisenberg Antiferromagnet, *Phys. Rev. X* **7**, 041072 (2017).
- [51] H. Shao and A. W. Sandvik, Progress on stochastic analytic continuation of quantum Monte Carlo data, *Physics Reports* **1003**, 1 (2023).
- [52] G. Schumm, S. Yang, and A. W. Sandvik, Cross validation in stochastic analytic continuation, *Phys. Rev. E* **110**, 055307 (2024).
- [53] S. Yang, G. Schumm, and A. W. Sandvik, Dynamic structure factor of a spin-1/2 Heisenberg chain with long-range interactions, *Phys. Rev. B* **111**, 224404 (2025).
- [54] G. Schumm, S. Zhang, and A. W. Sandvik, Single-particle dispersion and density of states of the half-filled two-dimensional Hubbard model, *Phys. Rev. B* **112**, 085109 (2025).
- [55] S. R. White and A. E. Feiguin, Real-Time Evolution Using the Density Matrix Renormalization Group, *Phys. Rev. Lett.* **93**, 076401 (2004).
- [56] E. Jeckelmann, Dynamical density-matrix renormalization-group method, *Phys. Rev. B* **66**, 045114 (2002).
- [57] S. Yang and A. W. Sandvik (2025), in preparation.
- [58] S. Yang and A. W. Sandvik, Spinons and Spin-Charge Separation at the Deconfined Quantum Critical Point (2025), [arXiv:2512.02962 \[cond-mat.str-el\]](https://arxiv.org/abs/2512.02962).
- [59] Y. Tang and A. W. Sandvik, Method to Characterize Spinons as Emergent Elementary Particles, *Phys. Rev. Lett.* **107**, 157201 (2011).
- [60] Y. Tang and A. W. Sandvik, Confinement and Deconfinement of Spinons in Two Dimensions, *Phys. Rev. Lett.* **110**, 217213 (2013).
- [61] C. K. Majumdar and D. K. Ghosh, On Next-Nearest-Neighbor Interaction in Linear Chain. II, *Journal of Mathematical Physics* **10**, 1399 (1969).
- [62] C. K. Majumdar, Antiferromagnetic model with known ground state, *Journal of Physics C: Solid State Physics* **3**, 911 (1970).
- [63] K. Okamoto and K. Nomura, Fluid-dimer critical point in $S = 1/2$ antiferromagnetic Heisenberg chain with next nearest neighbor interactions, *Physics Letters A* **169**, 433 (1992).
- [64] K. Nomura and K. Okamoto, Critical properties of $S = 1/2$ antiferromagnetic XXZ chain with next-nearest-neighbour interactions, *Journal of Physics A: Mathematical and General* **27**, 5773 (1994).
- [65] J. Wess and B. Zumino, Consequences of anomalous ward identities, *Physics Letters B* **37**, 95 (1971).
- [66] E. Witten, Global aspects of current algebra, *Nuclear Physics B* **223**, 422 (1983).
- [67] E. Witten, Non-abelian bosonization in two dimensions, *Communications in Mathematical Physics* **92**, 455 (1984).
- [68] A. W. Sandvik, Stochastic series expansion method with operator-loop update, *Phys. Rev. B* **59**, R14157 (1999).
- [69] A. W. Sandvik, Computational Studies of Quantum Spin Systems, *AIP Conference Proceedings* **1297**, 135 (2010).
- [70] A. Angelucci, Effective lattice actions for correlated electrons, *Phys. Rev. B* **51**, 11580 (1995).
- [71] M. Brunner, F. F. Assaad, and A. Muramatsu, Single hole dynamics in the one-dimensional t - J model, *The European Physical Journal B - Condensed Matter and Complex Systems* **16**, 209 (2000).
- [72] M. Brunner, F. F. Assaad, and A. Muramatsu, Single-hole dynamics in the $t - J$ model on a square lattice, *Phys. Rev. B* **62**, 15480 (2000).
- [73] E. Y. Loh, J. E. Gubernatis, R. T. Scalettar, S. R. White, D. J. Scalapino, and R. L. Sugar, Sign problem in the numerical simulation of many-electron systems, *Phys. Rev. B* **41**, 9301 (1990).
- [74] Y. Q. Qin, B. Normand, A. W. Sandvik, and Z. Y. Meng, Amplitude Mode in Three-Dimensional Dimerized Antiferromagnets, *Phys. Rev. Lett.* **118**, 147207 (2017).
- [75] K. Ghanem and E. Koch, Generalized maximum entropy methods as limits of the average spectrum method, *Phys. Rev. B* **108**, L201107 (2023).
- [76] I. Affleck, T. Kennedy, E. H. Lieb, and H. Tasaki, Rigorous results on valence-bond ground states in antiferromagnets, *Phys. Rev. Lett.* **59**, 799 (1987).
- [77] I. Affleck, T. Kennedy, E. H. Lieb, and H. Tasaki, Valence bond ground states in isotropic quantum antiferromagnets, *Communications in Mathematical Physics* **115**, 477 (1988).
- [78] S. Yang, D.-X. Yao, and A. W. Sandvik, Deconfined quantum criticality in spin-1/2 chains with long-range interactions (2020), [arXiv:2001.02821 \[physics.comp-ph\]](https://arxiv.org/abs/2001.02821).
- [79] R. O. Kuzian, R. Hayn, and J. Richter, Recursion method and one-hole spectral function of the Majumdar-Ghosh model, *The European Physical Journal B - Condensed Matter and Complex Systems* **35**, 21 (2003).
- [80] T. Tohyama and S. Maekawa, Effect of spin gap on single-hole excitation spectrum in the one-dimensional t - J - J' model, *Journal of Physics and Chemistry of Solids* **59**, 1864 (1998).
- [81] R. Hayn and R. O. Kuzian, Spectral function of one hole in several one-dimensional spin arrangements, *Phys. Rev. B* **62**, 12156 (2000).
- [82] C. Jurecka and W. Brenig, Single-hole dynamics in dimerized and frustrated spin chains, *Phys. Rev. B* **63**, 094409 (2001).